Kinematic and Precipitation Structure of the 10–11 June 1985 Squall Line

M. I. BIGGERSTAFF AND R. A. HOUZE, JR.

Department of Atmospheric Sciences, University of Washington, Seattle, Washington

(Manuscript received 8 November 1990, in final form 1 May 1991)

ABSTRACT

High-frequency (90 min) rawinsonde data from a special mesoscale network (26 sites) have been combined with wind profiler, dense automated surface network data (80 stations spaced 50 km apart), and a series of high-resolution dual-Doppler radar analyses in a common framework attached to a moving squall-line system to form a comprehensive dataset describing the mature phase of the 10–11 June 1985 squall line observed during PRE-STORM. The dual-Doppler radar analyses covered a 200 × 300 km^2 area, from the leading edge of the convective line to the back edge of the trailing stratiform precipitation region, thus, providing high-resolution wind information over a very broad portion of the storm system.

The comprehensive analysis is used to resolve several aspects of the trailing stratiform region that had remained unclear from previous studies. First, a difference in the horizontal scale was found between the mesoscale updraft, which at upper levels was on the scale of the trailing stratiform cloud, and the strong mesoscale downdraft, which at mid-to-lower levels was on the scale of the trailing stratiform precipitation. Second, the region of heaviest stratiform precipitation (the secondary band) was found to be immediately downwind of the most intense portions of the convective line, and the width of the trailing stratiform precipitation region was controlled by a combination of the wind velocity and microphysical fall-speed scales. Third, the radar reflectivity minimum observed at mid-to-lower levels in the region just behind the convective line was found to coincide with deep subsidence from mid-to-upper levels, which may have reduced the mass of the hydrometeors through sublimation and evaporation. However, precipitation trajectories computed from the comprehensive analysis indicate another contributing factor; namely, the source region of hydrometeors at low levels just behind the convective line was at a lower altitude than the source region of low-level hydrometeors in the heavy stratiform precipitation farther behind the convective line. Thus, even if all other factors had been the same, the hydrometeors in the heavy stratiform rain would have had more time to grow than those found in the region of the radar reflectivity minimum just behind the convective line. Moreover, hydrometeor detrainment may have been greater near cloud top than at lower levels.

1. Introduction

The Oklahoma–Kansas Preliminary Regional Experiment for Stormscale Operational Research Meteorology—Central Phase (PRE-STORM) was conducted during May and June of 1985 to study mesoscale convective systems (MCSs) (Cunning 1986); the type that are responsible for much of the warm season rainfall and severe weather over the central portion of the country (Fritsch et al. 1986). Of the several MCSs that were observed in PRE-STORM, the one that occurred on 10–11 June 1985 has been the most thoroughly studied. It consisted of a leading line of convection and a trailing region of stratiform rain. Early studies of storms of this type observed in midlatitudes were carried out by Newton (1950), Fujita (1955), and Pedgley (1962), and similar storms in the tropics were studied by Hamilton and Archbold (1945) and Zipser (1969). It is now known that the leading line of convection followed by a region of stratiform precipitation is a mode of storm organization frequently seen over the central United States (Houze et al. 1990). The leading line of convection and, to a lesser extent, the trailing region of stratiform rain in this type of storm have also been numerically simulated with considerable success (e.g., Dudhia et al. 1987; Nicholls 1987; Rotunno et al. 1988; Fovell and Ogura 1988, 1989; Redelsperger and Lafore 1988; Lafore and Moncrieff 1989; Tao and Simpson 1989).

Aspects of the large-scale kinematic structure of squall lines with a trailing region of stratiform rain have been documented observationally in past composite studies of soundings obtained from special mesoscale networks (Ogura and Chen 1977; Ogura and Liou 1980; Gamache and Houze 1982, 1985; Houze and Rappaport 1984; Leary and Rappaport 1987). However, because of the limited temporal and spatial resolution of sounding data, these studies do not show the mesoscale airflow patterns in much detail. Studies using Doppler radars have resolved the airflow patterns in squall-line systems on spatial scales of only a few

Corresponding author address: Dr. Michael I. Biggerstaff, Department of Meteorology, College of Geosciences, Texas A&M University, College Station, TX 77843.

kilometers and temporal scales of just a few minutes (Heymsfield and Shotz 1985; Smull and Houze 1985, 1987a; Srivastava et al. 1986; Kessinger et al. 1987; Chong et al. 1987; Roux 1988), but the time and area covered by the data in these studies were quite limited.

In these previous studies, datasets that would have allowed a combination of the large-scale spatial coverage of a rawinsonde network and the high resolution afforded by multiple-Doppler radar observations were not available. The design of the PRE-STORM observational network, however, made such a combination of data possible. A special rawinsonde network was established with two pairs of Doppler radars located within the network. Three experimental wind profilers were also added to the rawinsonde network, and automated surface stations were deployed over most of Oklahoma and Kansas with a spacing of just 50 km. An important aspect of this experimental arrangement was that the Doppler radars used in PRE-STORM were operated continuously during precipitation events. Moreover, the Doppler radars were operated to maximize coverage. This procedure deviated from many other programs in which Doppler radar scans were focused on a limited area and time to maximize detail. Hence, with PRE-STORM, it became possible to analyze a series of Doppler radar scans taken throughout the passage of a storm, and to combine that information with high-frequency rawinsonde and surface station measurements to build an extraordinarily comprehensive dataset on MCSs.

However, with such a comprehensive dataset, the assimilation of diverse types of information is itself a major problem. It is not surprising, therefore, that several studies of the 10–11 June 1985 storm have been made from subsets of the total information available. Smull and Houze (1987b) used single-Doppler radar data and Augustine and Zipser (1987) used profiler data to identify the "rear inflow jet" in this storm. Rutledge et al. (1988a) presented an overview of the radar-echo evolution and used single-Doppler radar data to document the vertical air motions in the stratiform region. Houze et al. (1989) presented a sample of the dual-Doppler analysis of the horizontal and vertical motions in the storm. Johnson and Hamilton (1988) analyzed sounding and surface data in the rear part of the storm to study the "wake low" that occurs at the back edge of this type of storm, and Johnson et al. (1990) used the soundings to diagnose vertical air motion at upper levels in the trailing stratiform cloud. Zhang et al. (1989), hereafter referred to as ZGP, simulated the 10–11 June 1985 storm in the context of a limited-area numerical weather prediction model and used several of the aforementioned studies for verification (ZGP; Zhang and Gao 1989). The verification was encouraging but severely limited by the lack of a detailed analysis of the whole dataset in any of the existing studies of this storm.

The objective of this study was to produce a comprehensive analysis of the kinematics and precipitation structure of the mature phase of the 10–11 June 1985 storm by combining a series of dual-Doppler analyses with high-frequency rawinsonde, profiler, and surface mesonet data in a time–space composite study. The dual-Doppler data were taken over a 3-h period during the storm's mature stage and, thus, covered the entire breadth of the storm from the leading line of convection to the back edge of the trailing stratiform rain region. By assimilating the sounding, profiler, surface mesonet, and dual-Doppler data into a single comprehensive analysis, we have produced a unique dataset that in future studies will allow detailed comparisons with model results, such as those of ZGP, and budget studies of heat, vorticity, and other quantities over a region, including the storm and its mesoscale environment.

In the present study, we present the basic fields of precipitation, horizontal wind, and vertical air motion that result from our comprehensive analysis. The overall consistency of the analysis will be demonstrated. Additionally, we will use this new and unique dataset to examine some outstanding problems regarding the structure of the squall line with trailing stratiform precipitation. We will focus on three aspects of the trailing stratiform region, which have remained unclear from previous studies.

The first aspect is the physical distinction between the mesoscale updraft and downdraft that dominate the circulation in the stratiform region. Vertical profiles of vertical motion in the stratiform regions of this type of storm always show descent on the order of tens of centimeters per second in the lower troposphere and ascent of similar magnitude in the upper troposphere (Houze 1989), but usually these profiles are determined over the same horizontal area. Past datasets have not allowed one to determine if the mesoscale updrafts and downdrafts are really features of the same scale or not. Both are mesoscale in horizontal dimension, but the factors controlling their scales appear to be quite different. Since numerical modeling studies (e.g., Fovell and Ogura 1988) and thermodynamic retrievals using Doppler data (e.g., Hauser et al. 1988) seem to indicate that the air in the trailing anvil is positively buoyant, it appears likely that the front-to-rear relative flow at upper levels advected positively buoyant air from the convective region rearward into the widespread trailing stratiform cloud layer. Moreover, it is reasonable to expect that this whole widespread buoyant layer will have a tendency to rise. Thus, a mesoscale updraft on the scale of the stratiform cloud might be expected. What controls the scale of the mesoscale downdraft is more difficult to evaluate a priori. Evaporation of falling precipitation into unsaturated air beneath the stratiform cloud creates negative buoyancy all across the region. Such evaporation is able to drive a mesoscale downdraft (Brown 1979); however, melting in the zone

of heavy stratiform rain also provides a significant contribution to cooling (Leary and Houze 1979). In examining selected profiles from the single-Doppler radar data for the 10–11 June 1985 storm, Rutledge et al. (1988a) found that the mesoscale downward motion in the stratiform region was strongest just beneath the melting layer. Because of the simultaneous extensive coverage and high resolution of both the wind and precipitation fields, we present further evidence that the precipitation exerts a strong control over the horizontal scale and intensity of the mesoscale downdraft. Since the heavy stratiform precipitation covers a smaller horizontal area, the region of *strong* mesoscale downdraft is smaller in horizontal scale than the mesoscale updraft.

The second aspect we consider is the precipitation structure in relation to the three-dimensional wind field. Is the horizontal scale of the trailing region of stratiform precipitation controlled by a fluid dynamical instability with some characteristic scale, or by the kinematics and microphysics of the storm? Analysis of the precipitation and wind fields, which were observed independently in the present study, suggests that the kinematics and microphysics of the storm are key factors. The horizontal distance and area over which ice particles generated in the convective line fall out is determined by the speed and direction of the upper-level flow and the fall speed of the ice particles—that is, by a combination of airflow and microphysical velocity scales. Rutledge and Houze (1987) confirmed this idea in a kinematic model of the stratiform region. Their calculations indicate that the particles being advected rearward grow substantially at the expense of vapor generated by ascent in the front-to-rear current, and that the total amount of the rainfall cannot be explained without this particle growth. However, the *position* of the heavy stratiform precipitation appears to be controlled by the kinematics. The dataset we have synthesized can be used to further test what controls the horizontal scale of the precipitation by examining the empirical relationship of the winds and precipitation in our composite analysis.

Another question regarding the stratiform precipitation region that has not been heretofore resolved is the reason for the minimum of reflectivity between the convective line and the region of heaviest stratiform rain. Houze et al. (1990) have found that this feature is quite common in mesoscale convective systems over Oklahoma. Two hypotheses have been considered in the past to explain this "reflectivity trough."[1] One suggestion is that the rain, graupel, and hail (if any) in the convective region have such large fall speeds that they fall out nearly vertically in the convective region, while the more slowly falling ice crystals in the upper regions of the convection are carried rearward a large distance before they melt, thus, leaving a minimum of reflectivity and rainfall at low levels just behind the convective line. The second hypothesis is that the minimum is associated with mean downward motion through a deep layer in this zone. The kinematic analysis of our comprehensive dataset shows that both of these processes occurred in the 10–11 June 1985 storm. However, precipitation trajectories from our analysis suggest that a third process was also active. Ice particles at the melting level above the heavy stratiform rain region apparently descended from the 150-mb level (storm top) of the convective region while ice particles at the melting level in the reflectivity trough apparently descended from only the 300-mb level of the convective region. Thus, particles in the reflectivity trough did not have as much time to grow as particles found at the same altitude in the heavy stratiform precipitation region. Moreover, the rearward flux of hydrometeors at 300 mb may have been different from that at 150 mb.

2. Data

a. Doppler radar

During the field phase of PRE-STORM four Doppler radars were deployed, two of which were the 5-cm wavelength Doppler radars (CP3 and CP4) operated by the National Center for Atmospheric Research (NCAR). These radars were located just west of Wichita, Kansas, on a 60-km north-northeast–south-southwest baseline. Rutledge et al. (1988a) provided details on the characteristics of the NCAR radars used during PRE-STORM. The other two radars were the 10-cm wavelength radars (NRO and CIM) operated by the National Severe Storms Laboratory (NSSL), which were deployed on a 40-km northwest–southeast baseline near Norman, Oklahoma. Figure 1 shows the location of the four Doppler radars along with the location of some of the National Weather Service (NWS) WSR-57 radars that were digitized in support of the PRE-STORM program. Of the four Doppler radars, only sets of coordinated plan-position indicator (PPI) scans from the two NCAR Doppler radars were used in this study. The storm did not come within range of the NSSL radars until the early dissipating stage of the convective line, and this analysis covers the mature phase of the storm. All of the aforementioned PPI scans, except for the one at 0510 UTC, were taken by sweeping azimuthally over a 360° conical surface. This procedure provided data for analyses on both sides (hereafter called the east and west lobes) of the north-northwest–south-southeast baseline (Fig. 1). Data are used from the scans beginning at 0209 UTC (east and west lobe), 0345 UTC (east lobe), 0414 UTC (west lobe), and 0510 UTC (east lobe). These scans were sufficient to provide high-resolution wind information

[1] The term "reflectivity trough" was coined by Sommeria and Testud (1988).

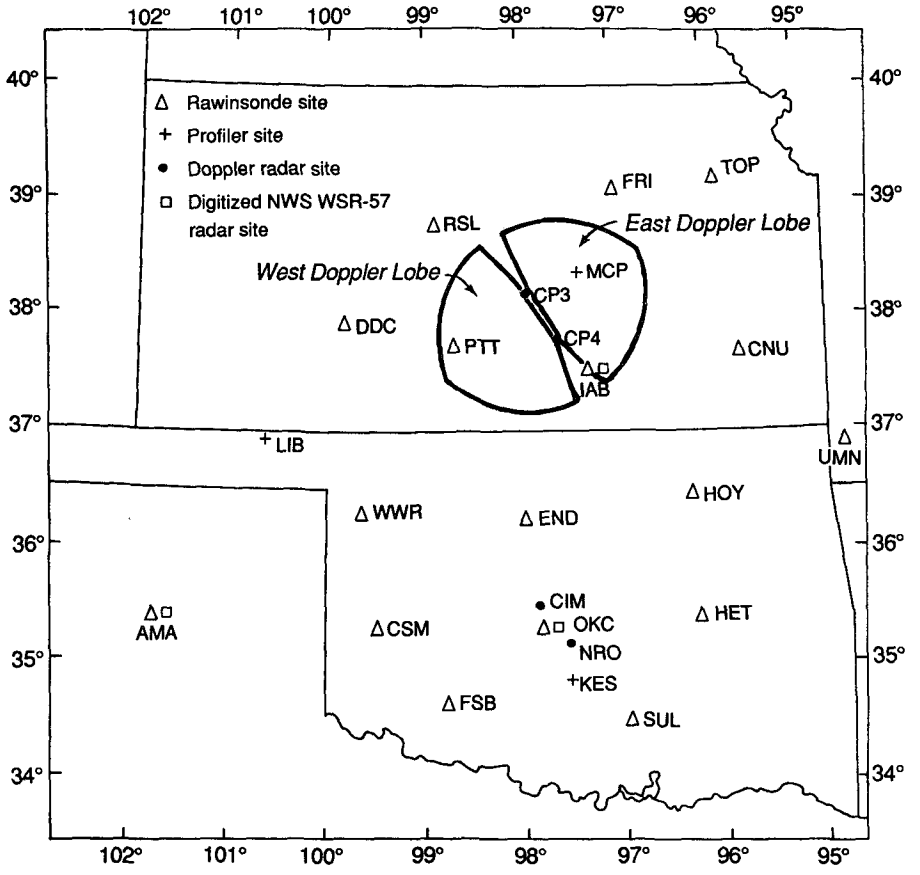

FIG. 1. PRE-STORM data network available during the 10–11 June 1985 storm.

completely across the storm system during its mature phase.

b. *Conventional radar*

Data collected from three digitized National Weather Service (NWS) surveillance (WSR-57) radars were used to determine the low-level reflectivity structure of the 10–11 June 1985 storm over a broader area than covered by the two NCAR Doppler radars. The 10-cm wavelength radars, with a 2° half-power beamwidth, were located at Wichita, Kansas (IAB), Oklahoma City, Oklahoma (OKC), and Amarillo, Texas (AMA) (Fig. 1).

c. *Rawinsonde*

The PRE-STORM upper-air network consisted of 14 NWS stations, 12 supplemental sounding sites, and 3 wind-profiling systems. Their locations are indicated in Fig. 1. The rawinsonde data were edited and interpolated to 150-m intervals at NSSL. Data from all the rawinsondes released in the PRE-STORM network between 0105 and 0600 UTC on 11 June 1985 were considered for use in the composite analysis.

d. *Profilers*

The profiler data were obtained from the Environmental Research Laboratory of the National Oceanic and Atmospheric Administration (NOAA/ERL). Vertical profiles of the horizontal winds at McPherson and Liberal, Kansas, were provided at 30-min intervals. Only those two of the three wind profilers shown in Fig. 1 were operating during the 10–11 June 1985 storm. Augustine and Zipser (1987) provided details on the resolution and other characteristics of the profilers used in PRE-STORM (see their Fig. 1). This study makes use of the 0230, 0330, 0430, and 0530 UTC soundings from the Liberal profiler and the 0100, 0230, 0330, 0430, and 0530 UTC soundings from the McPherson profiler.

e. *Surface mesonetwork*

An 84-station network of surface stations spaced roughly 50 km apart (Fig. 2) was installed and operated

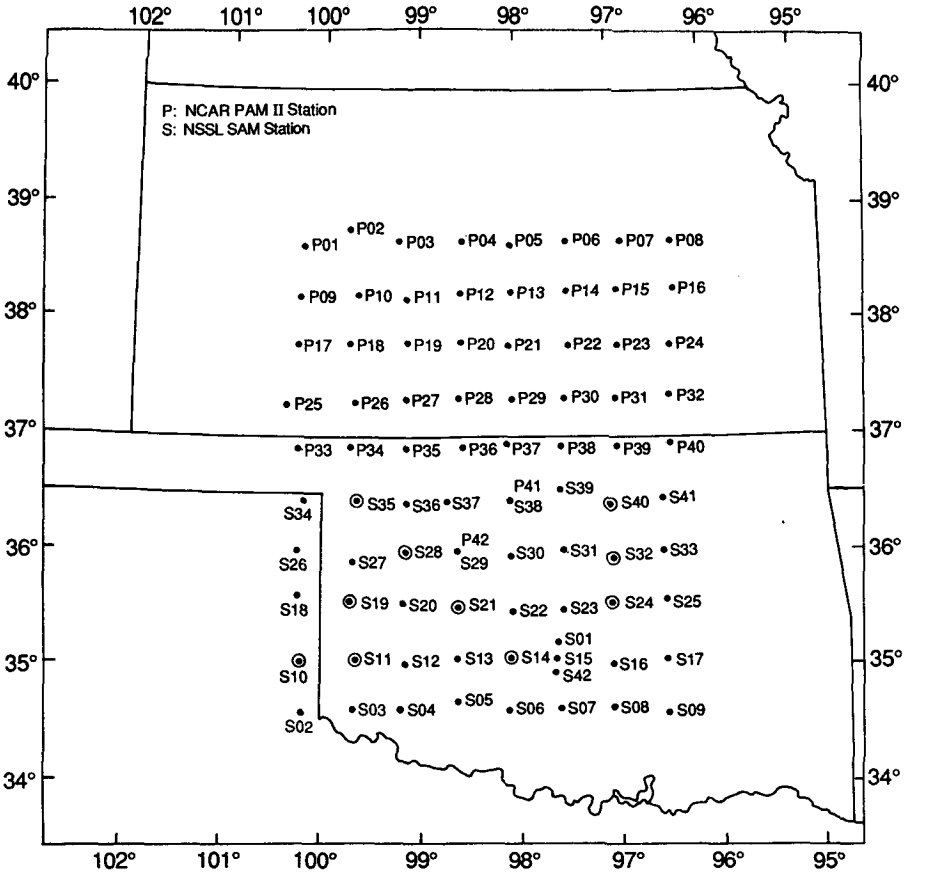

FIG. 2. PRE-STORM surface mesonetwork. Circled stations were not operating during the 10–11 June 1985 storm.

over Kansas and Oklahoma as one component of PRE-STORM (Johnson and Hamilton 1988). The Kansas portion of the network consisted of 42 NCAR Portable Automated Mesonetwork (PAM II) stations. The Oklahoma portion of the network consisted of 42 NSSL Surface Automated Mesonetwork (SAM) stations, although several were not in operation during the 10–11 June 1985 storm. The data from these stations were obtained from NOAA/ERL and consisted of 5-min-averaged thermodynamic and wind measurements and accumulated rainfall recorded at 5-min intervals. All available data between 0200 and 0630 UTC on 11 June 1985 were included in this study.

3. Method of analysis

a. Construction of the composite coordinate system

To construct a coordinate system attached to the moving storm, the leading edge of the 10–11 June 1985 squall line was tracked using the surface mesonetwork data and radar reflectivity from the three digitized NWS WSR-57 radars as the storm moved across the PRE-STORM network (Fig. 3). The northern portion of the squall line moved with an average speed of 14.5 m s^{-1}, while the central and southern portion of the line moved at average speeds of 18 m s^{-1} and 16 m s^{-1}, respectively. The directions of motion were roughly from 305° in each case. These values agree well with results from other studies of this squall line (Johnson and Hamilton 1988; Rutledge et al. 1988a; Smull and Houze 1987b).

To determine the storm motion most appropriate for the composite analysis, we followed the approach of Gamache and Houze (1982) and tracked the center of the squall line across the network to arrive at an overall storm motion of 18 m s^{-1} from 305°. The center of the squall line is defined as the point along the leading edge of the convective line that most nearly satisfies all of the following simultaneously: 1) the forwardmost point on the squall line, 2) the point that bisected the squall line, and 3) the point providing the smoothest motion from hour to hour.

For the 10–11 June 1985 storm, the selected point was at the central, or bowed-out, part of the convective line. Figure 3 shows the location of the center of the

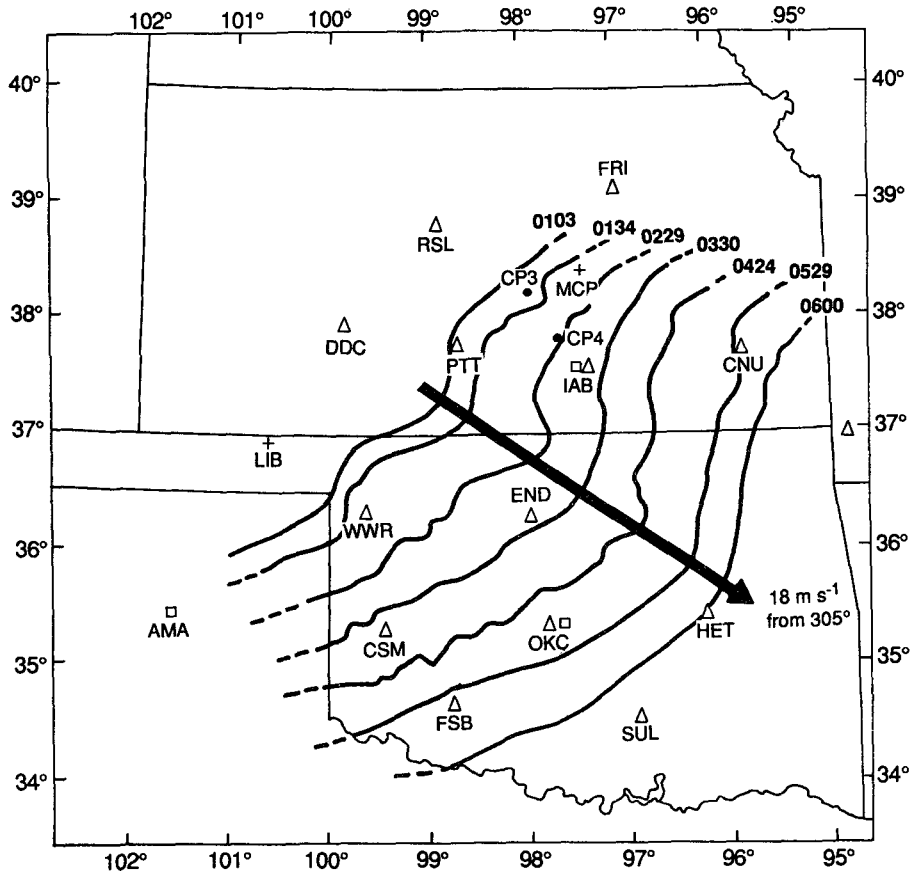

FIG. 3. Isochrones of the leading edge of the squall line during the composite time period. Dashes indicate that the true end of the squall line extended beyond that shown. The heavy, straight arrow indicates the location of the squall-line center (see text) as a function of time.

squall line as a function of time as the heavy straight line that roughly bisects the isochrones of the squall line position. The orientations of the axes of the composite coordinate system (Fig. 4) were determined by defining the positive X' axis to be in the direction of the storm-motion vector, toward 125° (the east-southeast). As a result, north is 35° counterclockwise from the positive Y' axis. For simplicity, the half of the squall line extending into the region of positive Y' will be referred to as the "northern" portion of the line, with the remainder referred to as the "southern" portion of the line.

b. The composite time frame

The majority of the data that were used in this study were collected between 0200 and 0500 UTC on 11 June 1985. As indicated by Fig. 5, this period straddled the peak in cold cloud-top temperatures associated with the mature phase of the squall-line system. Thus, this period represents the most steady part of the system's life cycle.

c. Processing of the horizontal wind data

Data from Doppler radars, profilers, rawinsonde soundings, and surface mesonet stations were all used in constructing the horizontal wind field in the composite analysis. However, each data type was analyzed separately before placing them into the composite framework. When data sources overlapped, the data closest to the mean analysis time of the composite were used.

1) DOPPLER RADAR

A complete dual-Doppler analysis was performed separately on each of the lobes of Doppler data used in the composite wind field. The dual-Doppler analysis was initiated by editing and unfolding all Doppler radar data using a version of the Research Data Support System (RDSS) software (Oye and Carbone 1981). Then the radial velocity and radar reflectivity from the two radars were interpolated onto a Cartesian grid with 1.5-km horizontal spacing and 0.5-km vertical spacing us-

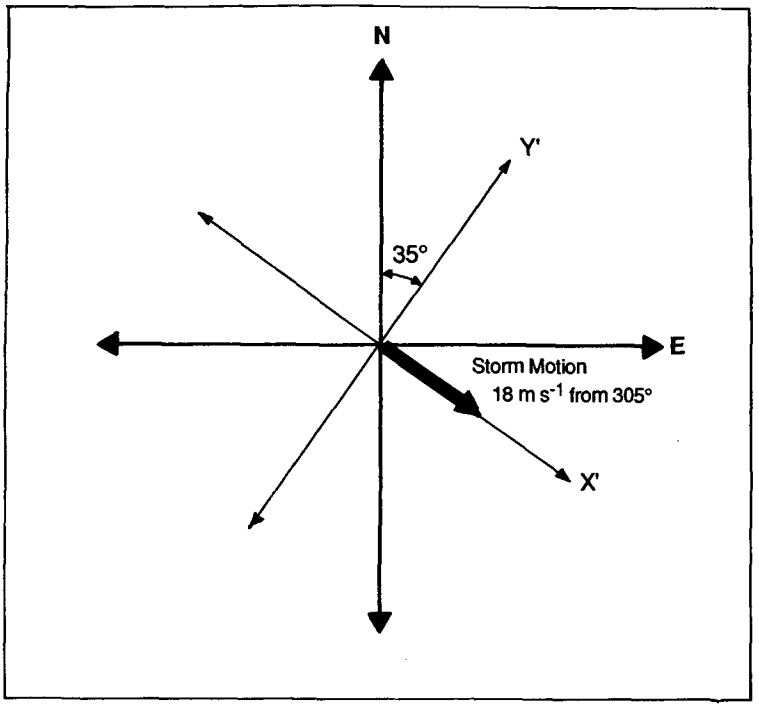

FIG. 4. Orientation of the composite coordinate system relative to true north.

ing the Sorted Position Radar Interpolation (SPRINT) software (Mohr et al. 1979). Further analysis was accomplished by using the Cartesian Editing and Display of Radar Data under Interactive Control (CEDRIC) software (Mohr and Miller 1983), which combined the two sets of radial velocities to produce estimates of the horizontal winds by assuming that the vertical motion was zero.

Particle fall speeds were then removed, following Marks and Houze (1987), using the reflectivity-weighted fall speed:

$$V_t = \left(\frac{\rho_0}{\rho}\right)^{0.4} [a(Z_e)^b]$$

$$\begin{cases} a = 2.6;\ b = 0.107 \text{ for water} \\ a = 0.817;\ b = 0.063 \text{ for ice.} \end{cases} \quad (1)$$

The effective radar reflectivity factor Z_e in standard units ($mm^6\ m^{-3}$) was taken to be the maximum of the two radar reflectivity estimates available at each grid point (one from each radar). The fall speeds are in units of meters per second. Density ρ was assumed to follow an exponential profile with a scale height of 10 km. The particles were assumed to be composed of ice for heights greater than 3.8 km above mean sea level (MSL) and liquid water for heights less than 3.4 km MSL. For the intermediate layer (just one grid level) an average of the two fall-speed estimates was used.

The horizontal wind components were patched to fill in well-bounded small holes, and a two-step filter (Leise 1981) was applied to all of the velocity data to remove wavelengths less than 6 km. Divergence was calculated and the anelastic continuity equation was applied to determine the vertical velocity. The boundary conditions used to integrate the continuity equation are discussed in appendix A.

Once the vertical velocities were determined, corrections were made to the horizontal winds from which new estimates of divergence and vertical velocity were obtained. This procedure was repeated until the mean of the absolute value of the change in the horizontal wind components at each level from one iteration to the next was less than 0.1 $m\ s^{-1}$.

The geopotential height data from nearby soundings were used to place the Doppler radar analyses, which were performed on constant height surfaces, into the pressure coordinates of the composite study. Then a time–space conversion (Fujita 1955) was used to place the Doppler-derived horizontal winds in the composite framework. In regions where the Doppler data overlapped, the analysis closest to the mean time of the composite (0330 UTC) was used. The effects of evolution on the composite analysis of the storm were thus reduced.

2) PROFILER

The profiler winds were plotted separately to check data quality. No suspect data were found for the profiler

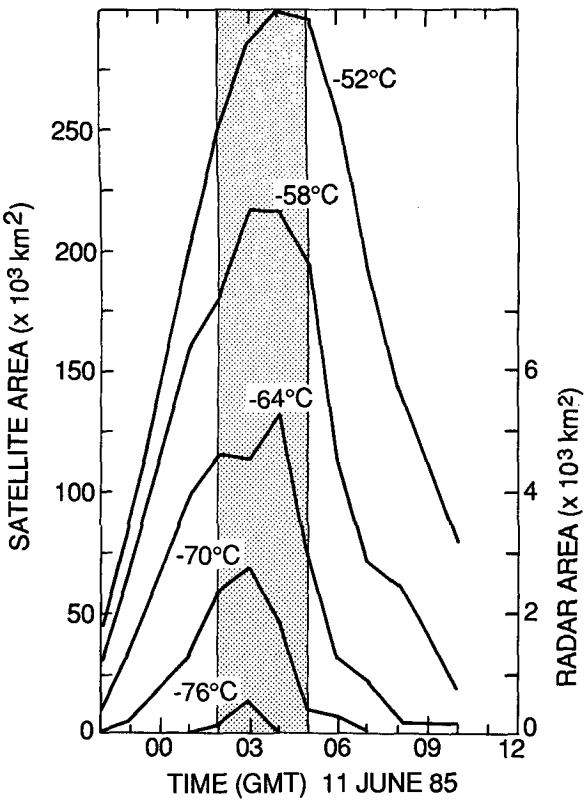

FIG. 5. Time variation of area covered by infrared temperatures lower than indicated values for the 10–11 June 1985 squall line. Shading indicates the period in which most of the data for the composite analysis were obtained. Adapted from Zipser (1988).

soundings used in this study. Geopotential height from neighboring rawinsondes were used to interpolate the profiler data, which were recorded at constant height levels to constant pressure surfaces. A time–space conversion was then used to place the profiler horizontal winds into the composite framework. The profiler winds agreed well with the dual-Doppler–derived winds in the regions where they overlapped.

3) RAWINSONDE SOUNDINGS

The rawinsonde-derived winds were plotted and checked for suspect data. All bounded layers of missing winds were filled in by assuming that the wind varied linearly with height. This procedure primarily affected soundings from the supplemental rawinsonde sites that had no wind information in the lowest 500 m above ground. Thus, the lowest half-kilometer of winds from some of the soundings were added by linearly interpolating between the ground and the next available wind. This procedure affected only the lowest 50 mb of the composite study. Once the rawinsonde data had been edited, it was interpolated to 25-mb intervals and placed in the composite coordinate system. The balloon drift was taken into account. Whenever two or more soundings were determined to be in virtually the same location relative to the squall line, the sounding closest to the mean analysis time was used. In all, 37 rawinsondes were used.

4) SURFACE MESONET STATIONS

Time-series plots for each automated surface station for both components of the horizontal wind from 0000 to 0700 UTC on 11 June 1985 were constructed to check for data quality. Suspect data were removed from the dataset. Afterward, all the recorded data were placed into the composite study by averaging all the values falling within each 15×15 km^2 grid box in the squall-line–relative coordinate system. Grid boxes without data were filled by using a scale-telescoped data-filling routine (Leise 1981), and then the data were filtered to remove wavelengths less than 45 km.

5) COMBINED HORIZONTAL WIND-FIELD ANALYSIS

After all the horizontal wind data were placed in the composite framework, streamline–isotach analyses were performed manually at the following levels: 900, 800, 675, 600, 550, 500, 400, 300, 200, and 150 mb. The surface analysis was performed objectively using standard NCAR data-plotting routines. These levels were selected to represent accurately the extended velocity–azimuth display (EVAD) analyses of divergence (Rutledge et al. 1988a). To derive other kinematic fields involving horizontal derivatives, the horizontal winds were manually digitized onto a 15×15 km^2 grid at each level. The wind components were filtered to remove wavelengths less than 60 km and then the derivatives were computed using standard finite-differencing methods.

d. Calculating the vertical wind

Divergence was obtained at representative levels using the aforementioned method. Vertical velocity ω was calculated from divergence by integrating the continuity equation,

$$\frac{\partial u}{\partial x} + \frac{\partial v}{\partial y} + \frac{\partial \omega}{\partial p} = 0 \qquad (2)$$

upward from the surface and using a modified O'Brien (1970) adjustment scheme (appendix B).

e. Processing of the thermodynamic data

Thermodynamic information was provided from two sources: rawinsonde soundings and surface mesonet stations. Each type of data was analyzed separately before being placed in the composite framework.

1) RAWINSONDE SOUNDINGS

All upper-air soundings were plotted on skew T–log p diagrams to check for suspect data. Soundings containing large superadiabatic lapse rates (SLRs) or other suspect data were removed. The exceptions to this were the 0105 UTC CSM and the 0400 UTC OKC soundings, where the SLRs were smoothed by linearly interpolating the temperature (as a function of height) using the temperature just above and just below the SLR and recomputing all the pertinent thermodynamic variables. The thermodynamic information from those two soundings was used with caution in the layers where the adjustments were made.

The thermodynamic data of the soundings were placed in the composite framework in the same manner as the horizontal wind data of the soundings. Contour analyses of several thermodynamic parameters were performed manually to study the thermodynamic structure of the squall-line system.

2) SURFACE MESOSNET STATIONS

The thermodynamic data of the surface mesonetwork were treated in the same manner as the wind data. However, the recorded surface pressures were adjusted to 518 m (the average height of the PRESTORM network) by making the corrections given in Johnson and Hamilton (1988) and then applying the hypsometric equation under the assumption that the virtual temperature was constant. The reduced pressures have a known accuracy of about 0.4 mb. Contour analyses of all composite surface thermodynamic fields were constructed using standard NCAR plotting routines.

4. Composite radar reflectivity pattern

To put the observed precipitation structure into the same framework as the other data, the radar reflectivity data recorded at AMA, OKC, and IAB were used to construct a composite of the radar reflectivity pattern for the 10–11 June 1985 storm. The reflectivity data from each radar were plotted on a common geographic map at 30-min intervals from 0130 to 0530 UTC (see Fig. 3 in Rutledge et al. 1988a for examples). These maps were then analyzed to determine the boundaries of the various reflectivity features that were to be placed in the composite coordinate system.

The geographic boundary for each map from 0130 to 0430 UTC of the convective region, identified as the leading area of reflectivity exceeding 35 dBZ, was then transferred into the composite coordinate system using the method outlined in section 3. Figure 6a shows the location of the convective region in the composite framework. The outer curve encloses the area formed by the union of all the transferred geographic boundaries. The composite framework extended slightly beyond the northern end of the convective line but did not enclose the southern end of the convective line. The convective region appeared to be wider at the northern and southern ends of the composite squall line because of the slower average storm speed for those parts of the storm. The inner curve encloses the area in which convective echo was observed for at least two hours during the 0130–0430 UTC time period. Regions of reflectivity are hatched if they exceed 50 dBZ for $\geq$2 h. Two regions of strong reflectivity occurred in the northern part of the convective line while an elongated region of strong reflectivity extended southward from the central, or bowed-out, part of the convective line. The remainder of the convective region was associated with apparently weaker radar reflectivity.

A broad region of stratiform precipitation was observed to the rear of the convective line during the mature stage of the squall-line system. The boundaries of the stratiform region, defined as all reflectivity greater than 15 dBZ not included in the convective region, were transferred into the composite coordinate system for each map from 0200 to 0500 UTC. Since the rearward edge of the stratiform region was beyond the maximum range of the recorded radar data at 0130 UTC, the slight shift in time from the convective region composite was necessary. The union of all the transferred stratiform boundaries is indicated by the outer curve in Fig. 6b. The inner curve encloses the area in which stratiform echo was observed for at least 2.5 h during 0200–0500 UTC. Since strong gradients of reflectivity were found along both the back edge of the echo pattern and the rear of the convective region, the size of the stratiform region was not sensitive to the 15-dBZ threshold.

An enhanced area of reflectivity, hereafter referred to as the *secondary band,* was located within the stratiform region. It marks the location of the most intense part of the surface stratiform precipitation. While the secondary band was found underneath an intense radar bright band observed at the melting level, the shape and position of the secondary band eliminates the possibility that this reflectivity enhancement was the result of an intersection between the radar's beam and the bright band at the melting level. Nor could it have been produced by attenuation, which is insignificant in moderate precipitation for 10-cm wavelength radars (Battan 1973). The secondary band was defined here as any area of reflectivity exceeding 25 dBZ within the stratiform region and surrounded by weaker echo. Figure 6c shows the area enclosed by the union of all the transferred boundaries (outer curve) and the area in which the secondary band was observed for at least 2.5 h during the 0230–0530 UTC time period (inner curve). Regions of reflectivity are hatched if they exceed 35 dBZ for $\geq$1.5 h during 0230–0530 UTC.

Figure 6d displays together the various parts of the composite radar reflectivity structure of the squall line.

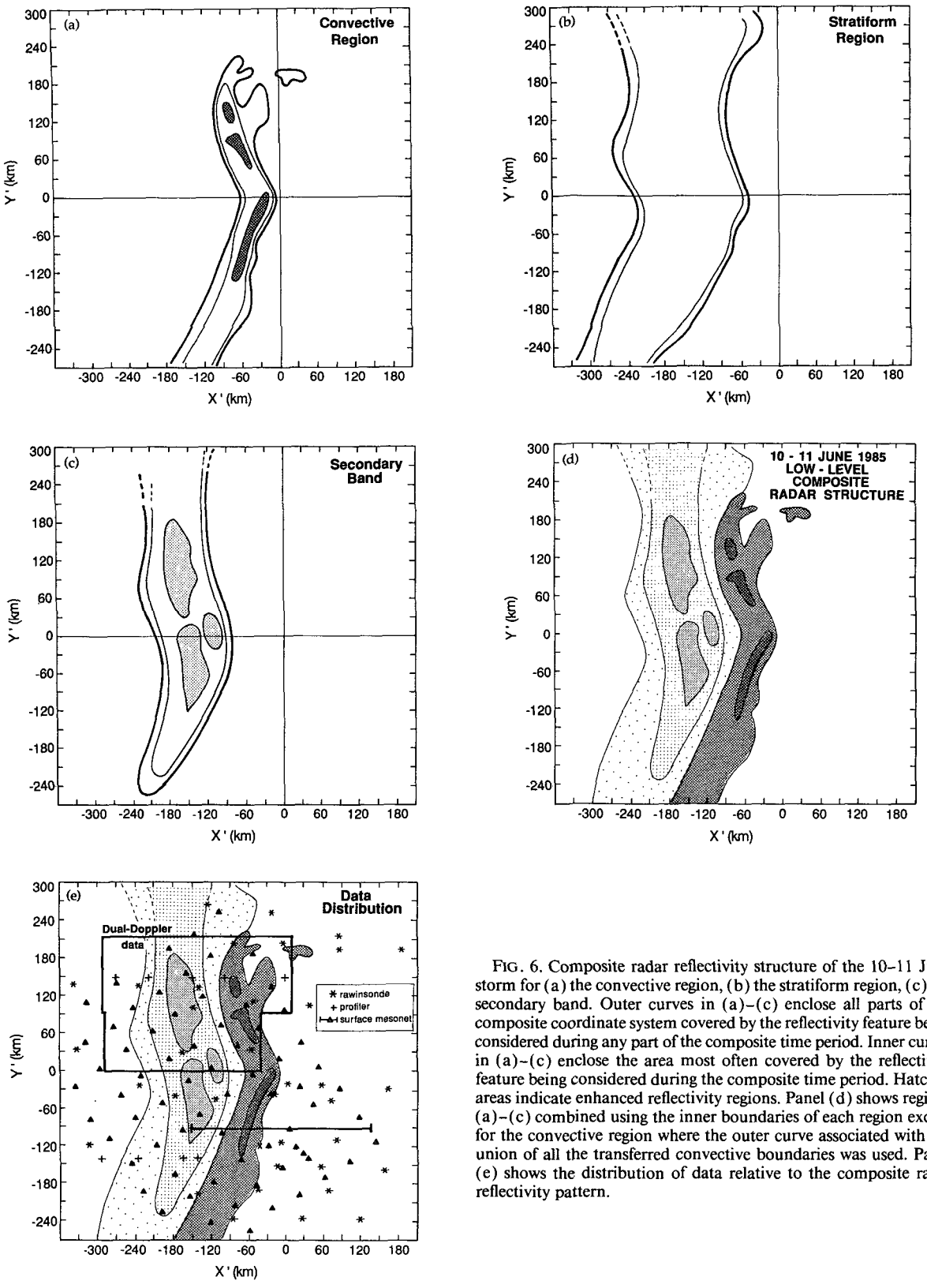

FIG. 6. Composite radar reflectivity structure of the 10–11 June storm for (a) the convective region, (b) the stratiform region, (c) the secondary band. Outer curves in (a)–(c) enclose all parts of the composite coordinate system covered by the reflectivity feature being considered during any part of the composite time period. Inner curves in (a)–(c) enclose the area most often covered by the reflectivity feature being considered during the composite time period. Hatched areas indicate enhanced reflectivity regions. Panel (d) shows regions (a)–(c) combined using the inner boundaries of each region except for the convective region where the outer curve associated with the union of all the transferred convective boundaries was used. Panel (e) shows the distribution of data relative to the composite radar reflectivity pattern.

The convective line was roughly 60 km wide and was followed by a region of stratiform precipitation about 150 km wide. Stratiform precipitation was also found to the north of the convective line. The secondary band, located within the stratiform region at a fairly constant distance from the rear of the convective line, was widest and best defined in the northern portion of the squall-line system. The enhanced regions of reflectivity within the secondary band were located directly to the rear of the enhanced regions of reflectivity within the convective line. Since each precipitation region was transferred into the composite coordinate system independently, the correspondence between the strongest reflectivities in the convective region and in the trailing stratiform region is especially significant. It will be shown later that this correspondence reflects the relationship between the upper-level storm-relative flow and the trailing stratiform precipitation of the storm.

The location of rawinsonde, profiler, and surface mesonet data and the region covered by dual-Doppler analyses in the composite coordinate system are shown with the radar reflectivity pattern in Fig. 6e. The pre-squall environment, the postsquall environment, and the precipitating portions of the MCS were evidently well sampled by rawinsondes. Unfortunately, many of the rawinsondes released in the stratiform region did not survive above the melting level; consequently, the distribution of data points at upper levels was not as good as that in Fig. 6e. The profiler data, however, provided excellent vertical cross sections of horizontal winds through the stratiform and postsquall regions. Moreover, the dual-Doppler analyses provided high-resolution coverage over the entire breadth of the northern half of the convective system.

5. Environmental characteristics

a. Developing stage

This storm developed in a weak baroclinic zone ahead of a surface cold front (Johnson and Hamilton 1988; ZGP). By 2100 UTC 10 June, the convective line was evident in the visible satellite imagery as an arc-shaped line of convective storms extending from the Texas–Oklahoma panhandles northward through western Kansas (see Fig. 6a in Johnson and Hamilton 1988). The convective line was well developed by 2200 UTC when it entered within the range of the NWS radar at Wichita, Kansas (Rutledge et al. 1988a). Since the 10–11 June 1985 storm formed to the west of the primary PRE-STORM mesonetwork between the standard synoptic-data collection periods, details of the environment ahead of the storm are not available. However, its general characteristics are probably well represented by the 2100 UTC 10 June WWR sounding (Fig. 7a), the earliest available for this case study, along the western edge of the PRE-STORM mesonetwork.

The lifting condensation level (LCL) and level of free convection (LFC) were 790 and 640 mb, respectively (for a parcel whose temperature and mixing ratio are the density-weighted average over the lowest 500 m). Evidently, deep lifting would have been required to bring the parcel to its LFC; however, the convective inhibition (CIN: Bluestein and Jain 1985) was only 77 J kg^{-1}. Thus, lifting in the vicinity of the surface front may have helped to initiate the squall line.

A minimum of 331 K in the vertical profile of equivalent potential temperature θ_e (Fig. 7b) was found at 450 mb in the environment where the storm was developing. The convective available potential energy (CAPE: Moncrieff and Miller 1976; Weisman and Klemp 1982) of the sounding was 1660 J kg^{-1}, which corresponds well to the typical CAPE associated with nonsevere, broken line-developing squall lines (Bluestein et al. 1987).

The magnitude of the low-level shear[2] (Fig. 7c) was about 5.0 m s^{-1} km^{-1} and was directed from 290°. However, the shear was not confined only to low levels of the environment. Since the westerly wind component remained nearly constant from 7 to 12 km, while the meridional component switched from light northerly to strong southerly flow, a southerly shear of about 4 m s^{-1} km^{-1} existed at upper levels. The lack of an extensive leading anvil in the 10–11 June 1985 storm is consistent with this upper-level "reverse shear" profile (Thorpe et al. 1982).

In a recent study of major rain events associated with MCSs over central Oklahoma, Houze et al. (1990) classified mesoscale precipitation systems (MPSs) according to their low-level radar reflectivity structure. Systems with a well-organized leading convective line trailed by stratiform precipitation were termed *strongly classifiable*. If the centroid of the stratiform precipitation was located directly behind the center of the convective line, then the MPS was termed *symmetric*. Employing their classification scheme, the 10–11 June 1985 storm was strongly classifiable and symmetric. The 2100 UTC WWR sounding exhibits many characteristics associated with the environment ahead of strongly classifiable symmetric storms. The wind profile shows pronounced turning of the winds with strong southerly flow at low levels veering to westerly flow at midlevels. Moreover, the across-line and along-line components of the density-weighted low-level wind shear, 4.0 and 2.8 m s^{-1} km^{-1}, respectively, were of similar magnitude.

b. Mature stage

As the storm evolved, it moved toward the east-southeast through the dense PRE-STORM mesonetwork. Rawinsondes released ahead of the storm reveal that there was considerable along-line variability in the

[2] The low-level shear is defined as the density-weighted vector difference between the winds at the surface and 2.5 km above the surface.

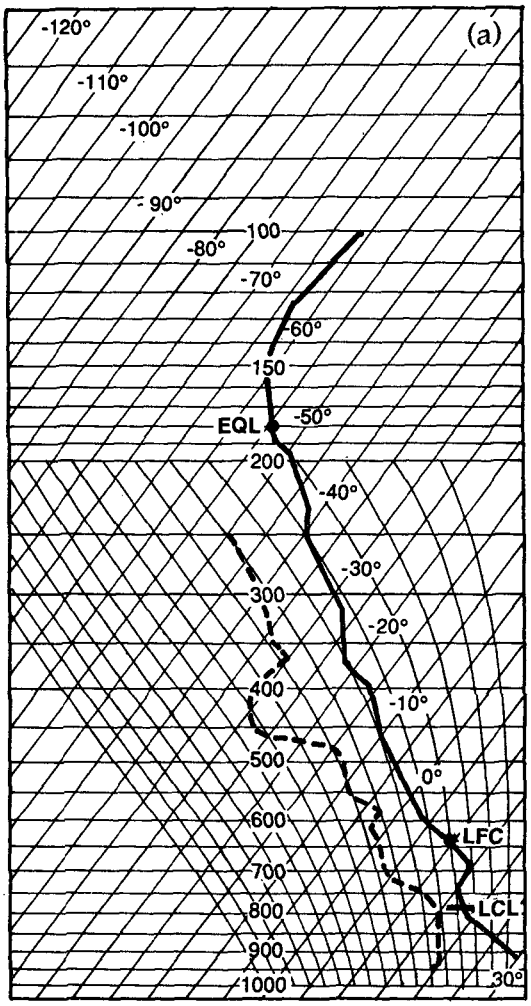

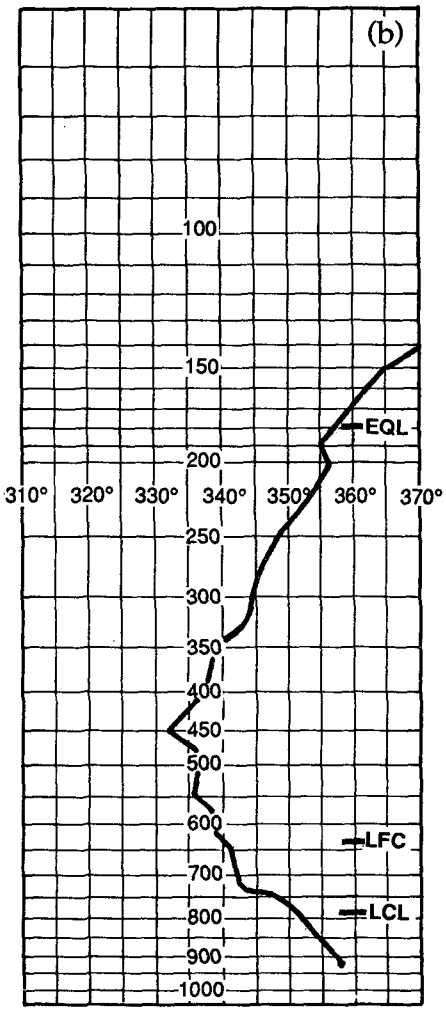

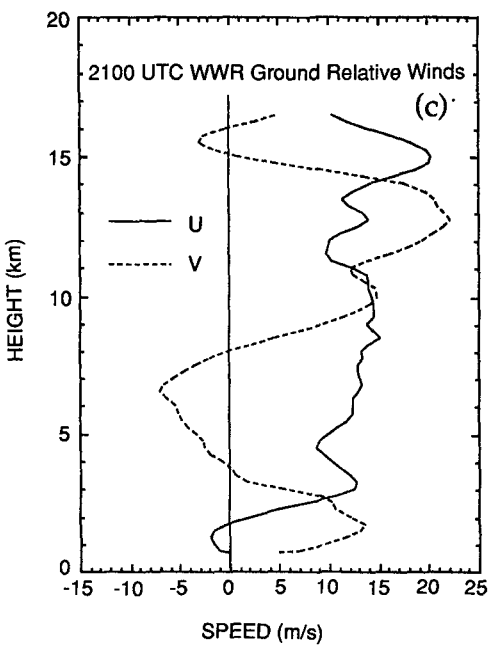

FIG. 7. WWR 2100 UTC 10 June 1985 (a) skew T–log p profile of temperature (solid) and dewpoint temperature (dashed), (b) equivalent potential temperature, and (c) ground-relative wind profile. The lifting condensation level (LCL), level of free convection (LFC), and equilibrium level (EQL) are indicated in panel (a) and (b). The numbers in (c) indicate height (km) above mean sea level.

thermodynamic and wind structure of the environment during the mature stage of the storm. These variations will be the subject of a future paper. Here we restrict ourselves to the large-scale characteristics of the environment of the mature system.

The environment ahead of the squall line during its mature stage is represented by the 0256 UTC SUL sounding shown in Fig. 8. Despite the low-level inversion, which resulted from strong nocturnal terrestrial cooling, the CAPE and CIN were 2040 J kg^{-1} and 60 J kg^{-1}, respectively, indicating that the environment ahead of the storm during its mature stage was roughly the same as during its developing stage. The lifted index for the 2100 UTC WWR sounding and the 0256 UTC SUL sounding were nearly identical: −6° versus −7°C.

However, significant differences are nonetheless evident between the 2100 UTC WWR and 0256 UTC SUL θ_e profiles (Figs. 7b and 8b). The minimum θ_e was 7 K lower at 0256 UTC and was found at 700 rather than 450 mb. This difference was associated with a drier 800–700-mb layer and much lower temperatures in the later sounding. The relatively low temperatures and the moist, stable planetary boundary layer associated with the 0256 UTC sounding are more characteristic of weakly classifiable (little linear organization to the convective region) and symmetric rather than strongly classifiable and symmetric storms (Houze et al. 1990). Moreover, the magnitude of the environmental low-level shear during the mature stage of the storm (Fig. 8c) apparently decreased to about half of what it was earlier. The across-line and along-line low-level shear were only 0.3 and 1.8 m s^{-1} km^{-1}, respectively. Thus, the characteristics of the environment associated with strong classifiability were lessening even though the bulk stability of the environment was little changed from 2100 to 0256 UTC.

6. Wind fields

a. Upper levels

The equilibrium levels of soundings discussed in section 5 indicate storm tops near 150 mb. The data coverage at this important level was somewhat reduced as a result of the weak radar echo at this altitude and some rawinsondes not reaching 150 mb. Nonetheless, 2 of the 5 dual-Doppler analyses and 23 of the 37 soundings contributed to the 150-mb analysis. Additionally, the wind profiler at Liberal added information in the southern portion of the composite domain.

The storm-relative streamline pattern determined from these data (Fig. 9a) is similar to the flow pattern obtained in Zhang and Gao's (1989) model simulation of the 10–11 June 1985 storm. The combination of the strong divergence from the MCS and the otherwise front-to-rear storm-relative environmental flow resulted in an area of weak rear-to-front flow through a portion of the convective region and a split in the presquall environmental flow. The flow resembled that obtained from a point source of divergence embedded in a translating fluid. The sharp turning of the streamlines and the stronger wind speeds in the northern half of the environment ahead of the storm were probably associated with another MCS, which was dissipating over eastern Kansas during the time period considered in this study (Rutledge et al. 1988a; ZGP). Behind the convective line, the flow was directed primarily front to rear, but had a strong along-line northward component in the northern half of the stratiform region. In the southern half of the storm, the front-to-rear flow was nearly perpendicular to the convective line but weaker than the flow to the north.

Strong divergence was found at 150 mb over both the convective and stratiform portions of the squall line (Fig. 9b); however, weak convergence was observed in both the presquall and postprecipitation regions. The convergence was slightly stronger in the presquall environment, a possible result of the juxtaposition of the 10–11 June 1985 storm and the earlier MCS. Associated with the convergence was subsidence near the rear of the stratiform region and in the presquall environment (Fig. 9c). Johnson et al. (1990) also diagnosed weak subsidence near storm top in the "rear stratiform region" for this case. The postprecipitation region in our composite domain corresponds closely to their rear stratiform region. We find that across the stratiform precipitation region itself, the vertical motion was apparently upward. Considering later stages of the storm, Johnson et al. (1990) diagnosed subsidence completely across the stratiform region at this level.

Below 150 mb, the storm-relative flow in the northern part of the stratiform region changed gradually to a more across-line orientation. At 300 mb, the relative flow was nearly straight back across the convective line (Fig. 10a). The direction of the flow through the stratiform region was nearly uniform; however, the wind speeds were greater in the northern portion of the stratiform region. Strong divergence was located over the convective region while weak divergence was found over most of the stratiform region (Fig. 10b). Some convergence was found over the central portion of the stratiform region as well as in the presquall and postprecipitation regions. Subsidence occurred in the presquall and postprecipitation regions in concentrated bands close to the edges of the squall-line system (Fig. 10c). The concentration of descent around the edges of mesoscale systems has been noted previously in observations (Hoxit et al. 1976) and mesoscale model simulations (Fritsch and Chappell 1980). A smaller and weaker region of subsidence was found between the convective line and the enhanced portions of the secondary band in the northern part of the squall-line system. Strong ascent was observed elsewhere throughout the MCS.

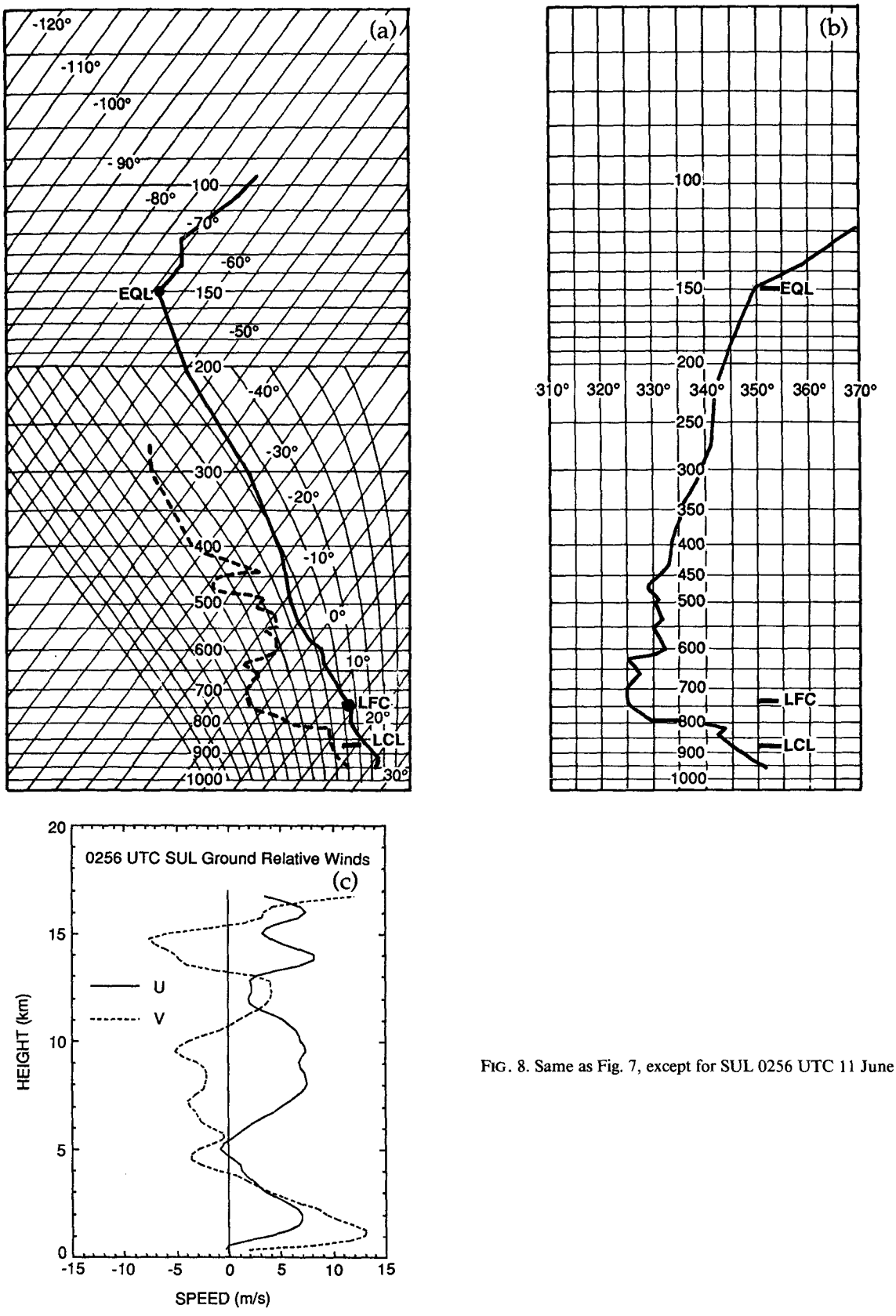

FIG. 8. Same as Fig. 7, except for SUL 0256 UTC 11 June 1985.

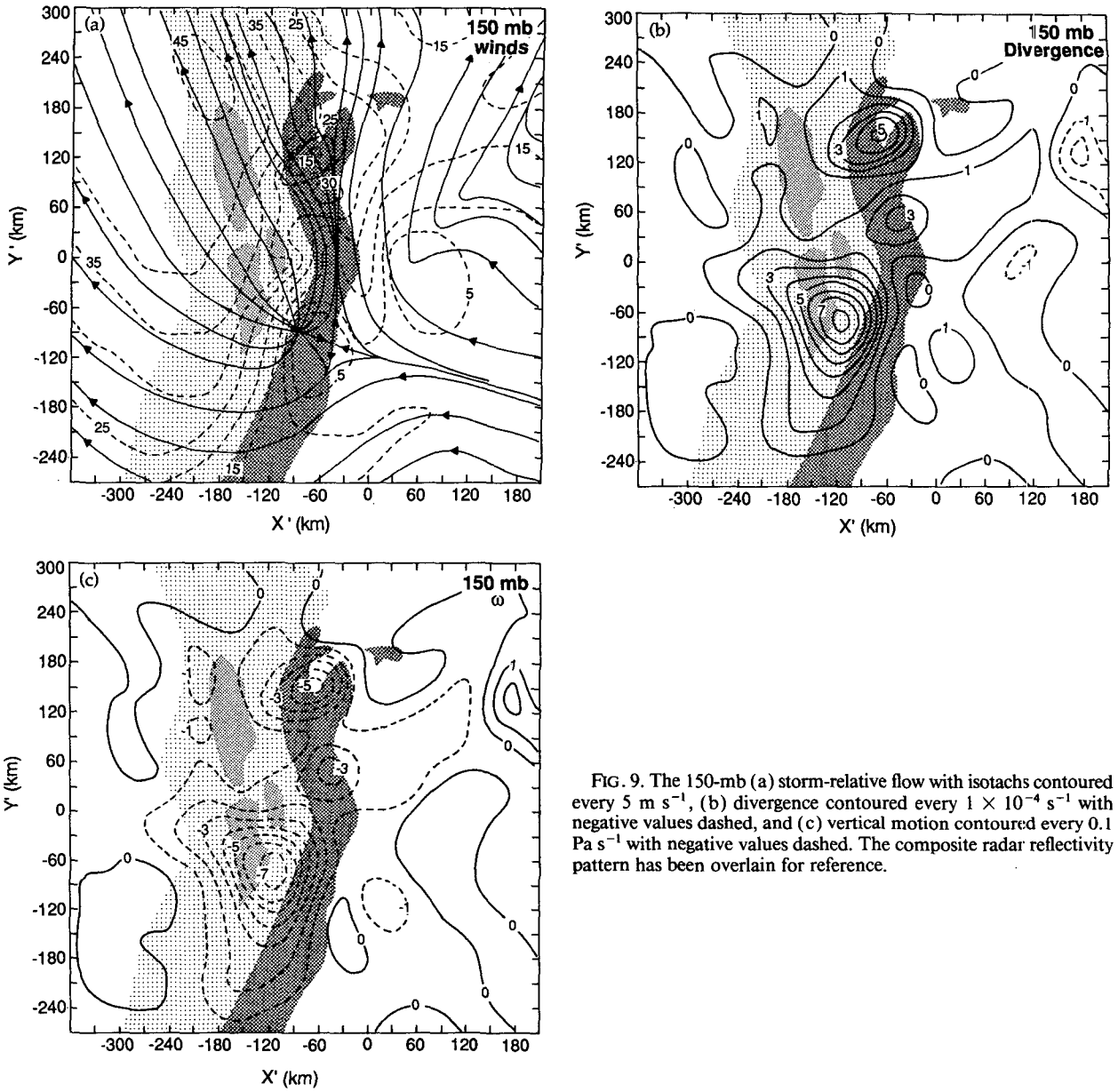

FIG. 9. The 150-mb (a) storm-relative flow with isotachs contoured every 5 m s^{-1}, (b) divergence contoured every 1×10^{-4} s^{-1} with negative values dashed, and (c) vertical motion contoured every 0.1 Pa s^{-1} with negative values dashed. The composite radar reflectivity pattern has been overlain for reference.

b. Midlevels above the melting band

At 400 mb, the front-to-rear flow was rather uniform in direction (Fig. 11a); however, the flow was much stronger and extended much farther beyond the rear of the convective line in the northern part of the system than elsewhere. A northward, primarily along-line flow was found behind the region of precipitation. This part of the postsquall environmental circulation had a weak rear-to-front component of motion over most of the postprecipitation region. Convergence was found generally along the interface of the front-to-rear and postsquall northward flows and over most of the stratiform region, but was strongest in the northern part of the postprecipitation region (Fig. 11b). Divergence was found over the northern part of the enhanced portion of the secondary band and over most of the convective region. Upward motion occurred in the convective and stratiform regions, except where, notably, subsidence was observed between the convective line and the enhanced portion of the secondary band in the northern half of the stratiform region (Fig. 11c). Like that found at 300 mb, bands of subsidence also were ahead of the convective line and to the rear of the stratiform precipitation region.

Low θ_e values, 330–335 K, were associated with the postsquall environmental flow (Fig. 11d). The lowest θ_e values in the postprecipitation region were found in

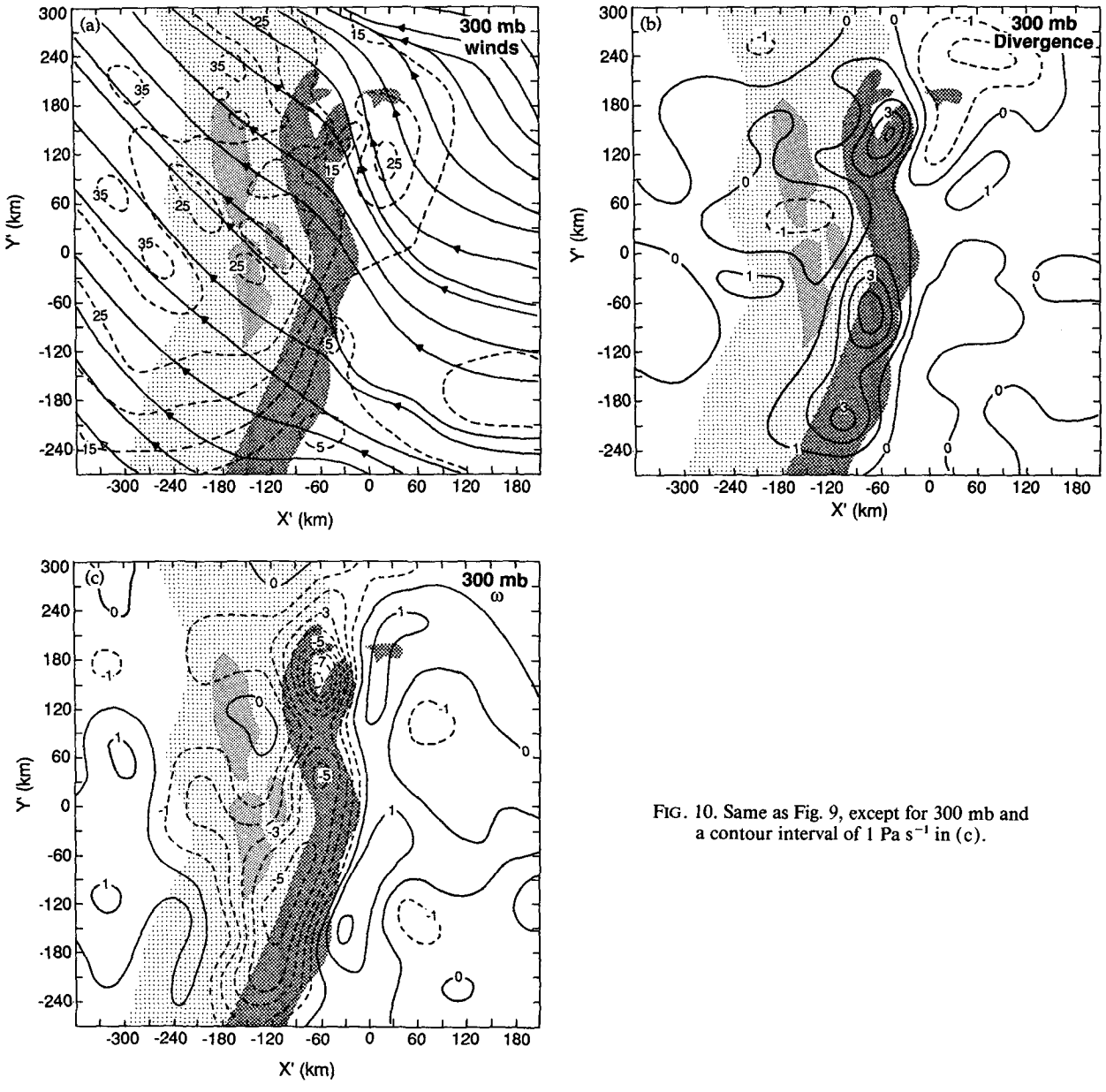

FIG. 10. Same as Fig. 9, except for 300 mb and a contour interval of 1 Pa s^{-1} in (c).

the northern part of the postsquall environmental flow where the relative humidity, with respect to ice, was only 75%. In the remainder of the postprecipitation and stratiform regions, the air was saturated with respect to ice. Thus, the postsquall environmental flow in the northern part of the analysis domain was associated with relatively dry, subsiding low-θ_e air.

At 500 mb, the postsquall environmental flow had a significant component perpendicular to the back edge of the squall-line system (Fig. 12a). Strong convergence between this *rear inflow* and the front-to-rear flow was concentrated near the back edge of the surface precipitation pattern (Fig. 12b). In the northern half of the squall-line system, a sharp line marked a sudden transition from front-to-rear flow across the stratiform region to the rear inflow from the postprecipitation region. Although this sharp transition was located roughly 200 km behind the leading edge of the convective line, it was oriented nearly parallel to the convective rainband. Smull and Houze (1987b) and Rutledge et al. (1988a) previously showed that the 10–11 June 1985 storm contained a strong rear-inflow current at midlevels below 500 mb throughout the stratiform rain region. It appears that part of the strength of the rear-inflow current in this case was because of the favorable rear-to-front environmental flow in the postprecipitation region. It has been suggested that the difference in flow between the postsquall and presquall environ-

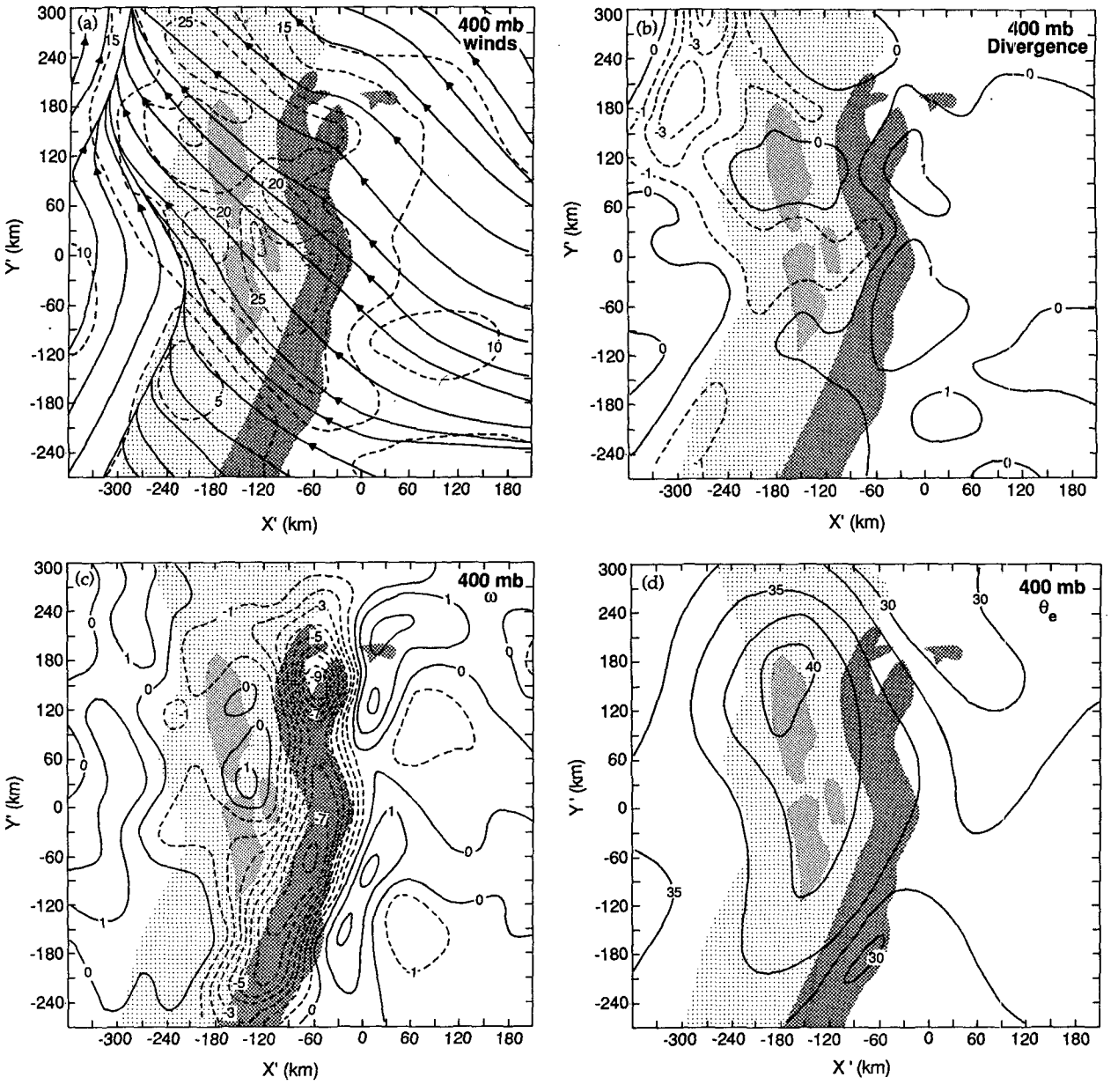

FIG. 11. The 400-mb (a) storm-relative flow with isotachs contoured every 5 m s^{-1}, (b) divergence contoured every 1 × 10^{-4} s^{-1} with negative values dashed, (c) vertical motion contoured every 1 Pa s^{-1} with negative values dashed, and (d) equivalent potential temperature contoured every 5 K with the leading 3 omitted on the labels. The composite radar reflectivity pattern has been overlain for reference.

ments was affected by large-scale baroclinity over the PRE-STORM area during the development of the 10–11 June 1985 storm (Johnson and Hamilton 1988; ZGP).

The streamline pattern at 500 mb also indicates that the front-to-rear flow was not as uniform at this level as it was aloft. In particular, the across-line component of flow was weak in the southern half of the stratiform region while it was strong to the north. In contrast to the strong convergence along the back edge of the northern part of the storm system, the southern portion of the storm was associated with only weak convergence. In general, the circulation at mid-to-upper levels appears to have been stronger in the northern half of the storm where data coverage was best. Comparisons between the profiler data collected at MCP and LIB (Augustine and Zipser 1987) also indicate that the relative flow was weaker in the southern portion of the stratiform region.

A series of mesoscale regions of upward and downward motion were found across the northern portion of the squall-line system at 500 mb (Fig. 12c, between

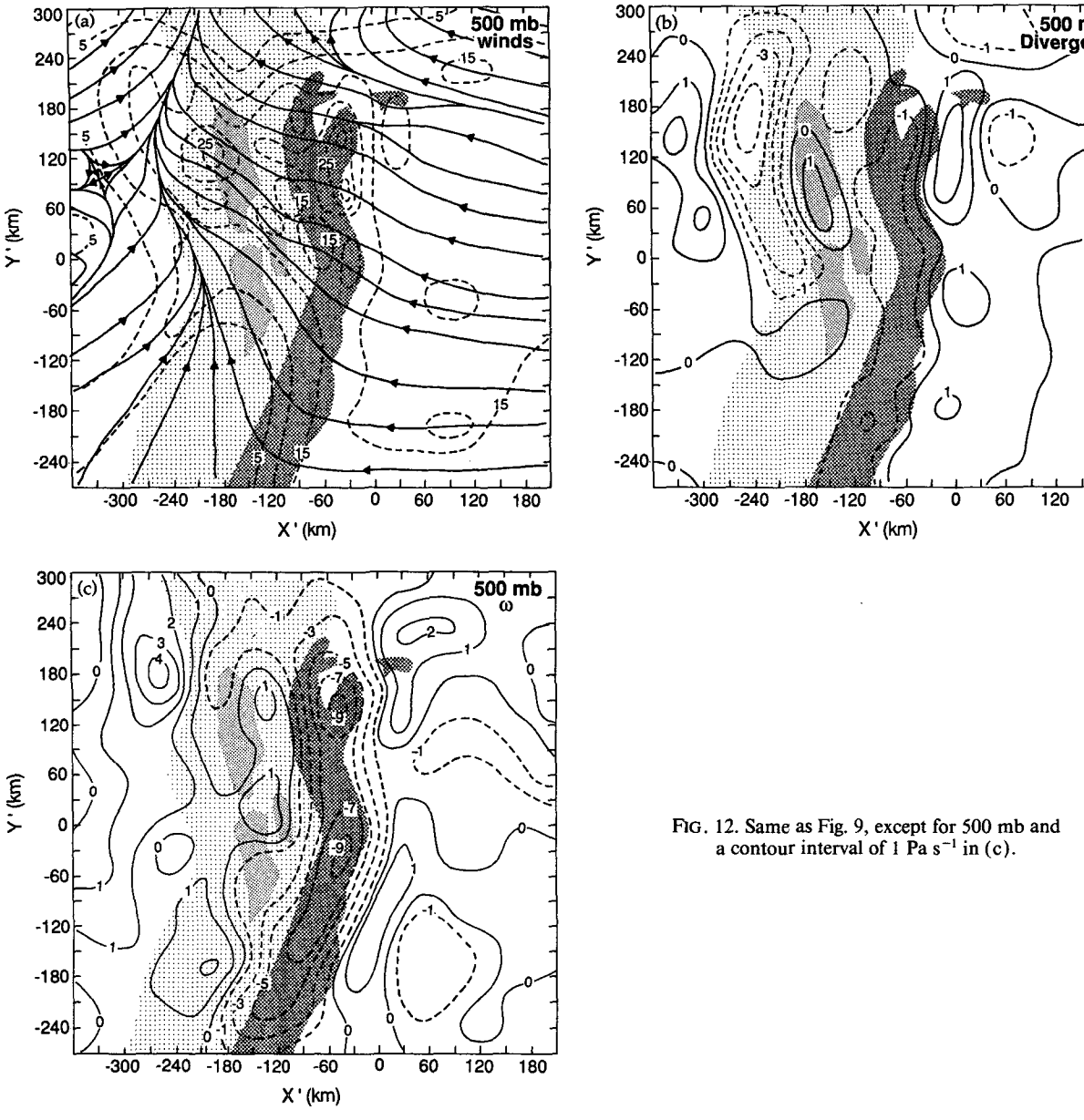

FIG. 12. Same as Fig. 9, except for 500 mb and a contour interval of 1 Pa s^{-1} in (c).

Y′ = 70 and 150 km). In the presquall environment, a mesoscale region of descent was observed[3] immediately ahead of the convective line (as at 300 and 400 mb), followed by an area of strong ascent associated with the convective line. Behind the convective line and ahead of the enhanced parts of the secondary band, a narrow region of descent was observed, followed by an area of weak ascent found over the remainder of the stratiform region. Farther to the rear of the system, at the back edge of the surface rainfall pattern, a mesoscale region of strong descent was observed. Except for the downward motion in the reflectivity minimum between the convective line and the enhanced portions of the secondary band, this pattern of vertical motion is consistent with that inferred in previous studies of squall lines with trailing stratiform precipitation. The effect of the mid-to-upper-level downdraft observed behind the convective line on the reflectivity structure of the storm will be discussed further in section 9e.

[3] Filtering of strong convective motions broadened the updraft associated with the convective line and shifted the boundaries of the subsidence away from the convective region. Thus, subsidence was probably located closer to the edges of the convective line than indicated here.

c. Midlevels below the melting level

The flow at 675 mb, which was about 600 m below the 0°C level in the stratiform precipitation region, had a detailed but nevertheless orderly structure (Fig. 13a). Two separate and apparently closed circulations were evident at this level. The broader of these was a cyclonic vortex centered near the back edge of the secondary band in the central part of the storm. Previous studies have shown that cyclonic circulations at midlevels often occur in the stratiform regions of MCSs (e.g., Gamache and Houze 1982; Leary and Rappaport 1987; Houze et al. 1989; Brandes 1990). The other closed-circulation feature was a relatively small-scale anticyclonic vortex observed near the front of the northernmost enhanced part of the secondary band. This anticyclonic vortex was part of a much larger-scale band of anticyclonic vorticity, which lay between the secondary band and the rear of the convective line. To date, no other observational study has shown a band of anticyclonic vorticity in this part of the stratiform region of a squall-line system. In fact, the overall vorticity structure of the storm at this level (Fig. 13b) is significantly different from that previously indicated for squall lines with trailing stratiform precipitation regions (e.g., Gamache and Houze 1982; Brandes 1990). A more thorough discussion of the vorticity structure of this storm is presented in Biggerstaff and Houze (1991a).

Although some divergence was found between the enhanced part of the secondary band and the rear of the convective line, the flow throughout the stratiform region was mostly convergent (Fig. 13c). In contrast, the airflow through the postprecipitation region was primarily divergent. Strong convergence and upward motion (Fig. 13d) were observed within the convective region, while subsidence was observed elsewhere, especially in the heavy stratiform precipitation regions.

Two strong mesolows, evident in the geopotential height field (Fig. 13e), were present in the northern portion of the squall-line system at this level. An intense mesolow associated with the convective region was near the northern end of the convective line. Circulation into this mesolow apparently brought some air from north of the storm into the system in the along-line direction. Some of the convergence observed in the northern end of the system was associated with this along-line flow. An apparently weaker but broader mesolow was found near the back edge of the stratiform region, with a trough extending southward along the back edge of the surface precipitation pattern. This trough and mesolow may have been partially responsible for the broad-scale rear-to-front flow observed throughout the storm. The rear-to-front flow was strongest in the northern half of the storm system where the across-line height gradients were strongest.

A weak ridge lay between the two strong mesolows. While the ridge was best defined in the central portion of the storm system, it extended all along the storm between the convective line and the heavy stratiform precipitation region. Thus, at this level, the ridge was located in approximately the same position as the band of anticyclonic vorticity seen in Fig. 13b. Moreover, both of these features appeared to be slightly ahead of the strongest downward motion within the storm at midlevels.

d. Lower levels

The 800-mb storm-relative streamlines (Fig. 14a) had considerably more uniformity in the along-line direction than at 675 mb; however, important along-line gradients nonetheless remain. In particular, a broad-scale cyclonic circulation was observed near the northern end of the convective line in association with the intense mesolow (Fig. 14b). The northern branch of the cyclonic circulation consisted solely of front-to-rear relative flow. Rear-to-front flow at this level was most intense and perpendicular to the convective line in the central, or bowed-out, part of the storm. This structure contrasts with that found at higher levels, where the rear-to-front flow was strongest in the northern part of the system with only weak rear-to-front flow in the central part of the storm. Hence, it is apparent that the bowed-out structure of the central part of the convective line was associated with strong rear-to-front flow at *lower levels* in that part of the storm.

The rear-to-front flow in the central part of the storm at 800 mb may have been influenced or aided by the across-line height gradient between the mesohigh underneath the enhanced portion of the secondary band and a mesolow near the front of an enhanced portion of the convective line (Fig. 14b). In their discussion of the simulated 10–11 June 1985 storm, Zhang and Gao (1989) suggested that the low-level mesohigh in the stratiform region was important to the development of the rear-to-front relative flow.

This effect on the rear inflow would be confined to low levels. As already shown, the rear-to-front flow associated with the 10–11 June 1985 storm extended to nearly 400 mb, and a well-defined mesolow was present at midlevels near the back of the northern half of the storm where the rear inflow was strongest. As suggested previously, part of the rear-to-front flow (i.e., at midlevels and farther back) may have been associated with the midlevel mesolow in the stratiform region and influenced by large-scale baroclinity. At 800 mb, the rear-to-front flow was apparently aided by a low-level height gradient between a mesohigh associated with the secondary band and a mesolow near the front of the convective line. However, the present analysis and the model simulation discussed by Zhang and Gao (1989) were incapable of resolving small-scale pressure perturbations that are often associated with convective lines (LeMone 1983). These pressure perturbations may also have influenced the rear-to-front flow at levels

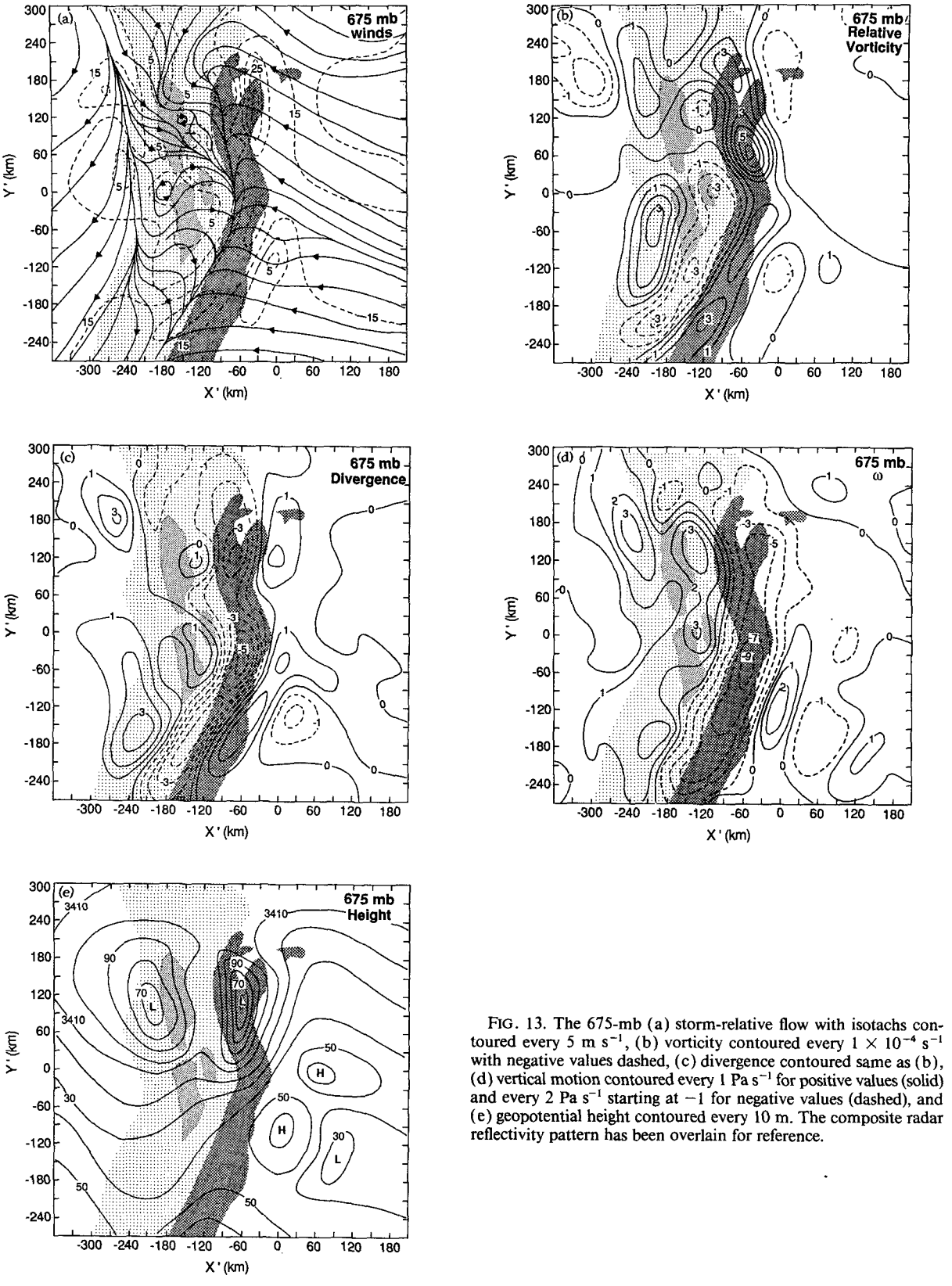

FIG. 13. The 675-mb (a) storm-relative flow with isotachs contoured every 5 m s^{-1}, (b) vorticity contoured every 1×10^{-4} s^{-1} with negative values dashed, (c) divergence contoured same as (b), (d) vertical motion contoured every 1 Pa s^{-1} for positive values (solid) and every 2 Pa s^{-1} starting at -1 for negative values (dashed), and (e) geopotential height contoured every 10 m. The composite radar reflectivity pattern has been overlain for reference.

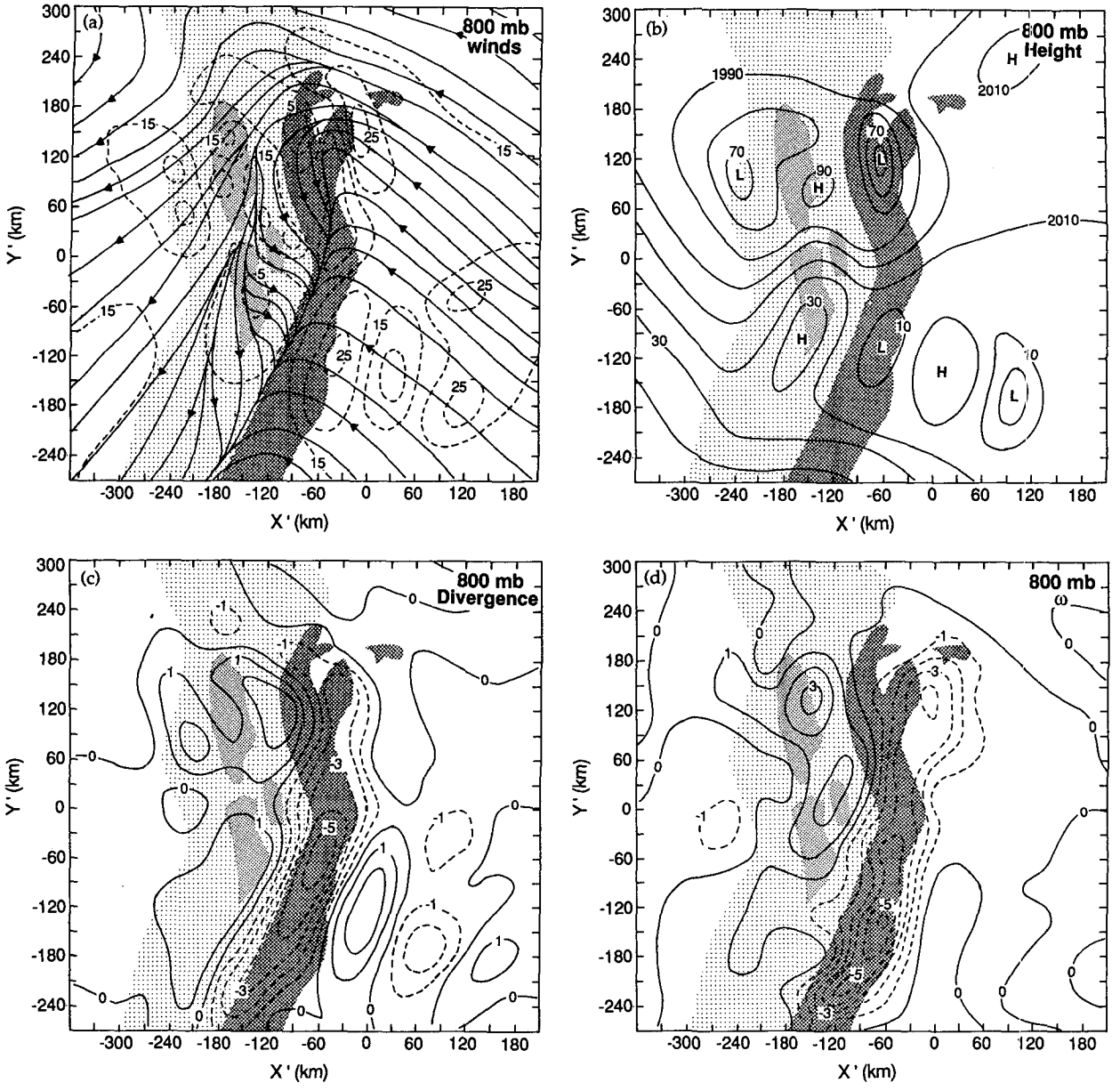

FIG. 14. The 800-mb (a) storm-relative flow with isotachs contoured every 5 m s^{-1}, (b) geopotential height contoured every 10 m, (c) divergence contoured every 1×10^{-4} s^{-1} with negative values dashed, and (d) vertical motion contoured every 1 Pa s^{-1} with negative values dashed. The composite radar reflectivity pattern has been overlain for reference.

near 800 mb, as indicated by the two-dimensional nonhydrostatic modeling study of Fovell and Ogura, (1989) who obtained a storm-relative rear-to-front flow near the convective line in response to a low pressure perturbation in the convective region. Thus, it appears that several processes are active in MCSs that affect the development of storm-relative rear-to-front flow across the whole storm.

Figure 14c shows that divergence was prevalent throughout the stratiform region at lower levels, while strong convergence characterized the convective region. The 800-mb vertical-motion field (Fig. 14d) reveals that subsidence occurred throughout the stratiform region. As at the 675-mb level, the subsidence appears to be enhanced near the heavy stratiform precipitation regions.

e. Surface level

The surface-level storm structure was determined from analysis of the surface mesonet data. Figure 15a shows that the storm-relative flow at this level was front-to-rear everywhere. It is apparent from the pattern of θ_e (Fig. 15e) that the relative streamlines ahead of the

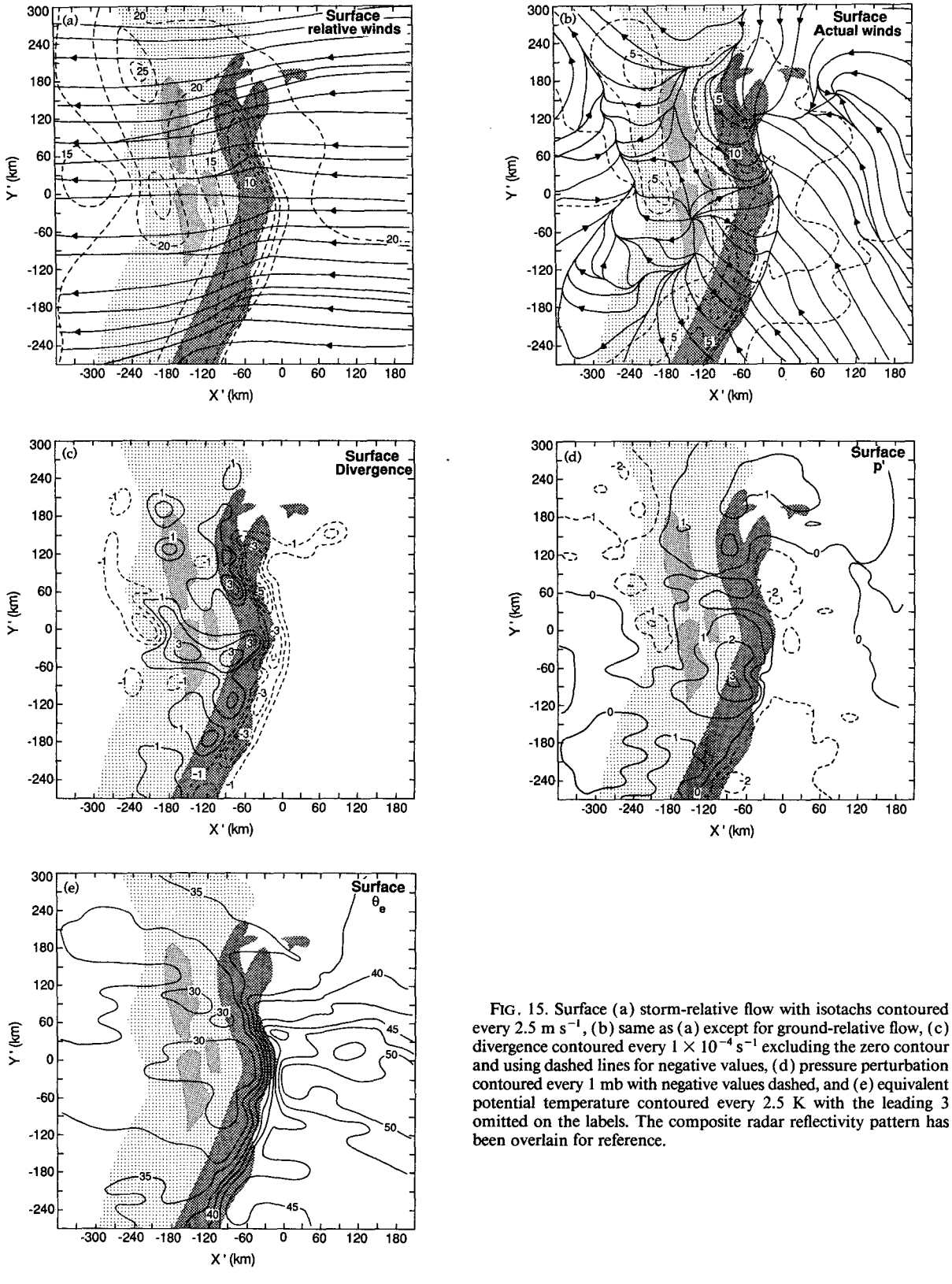

FIG. 15. Surface (a) storm-relative flow with isotachs contoured every 2.5 m s^{-1}, (b) same as (a) except for ground-relative flow, (c) divergence contoured every 1×10^{-4} s^{-1} excluding the zero contour and using dashed lines for negative values, (d) pressure perturbation contoured every 1 mb with negative values dashed, and (e) equivalent potential temperature contoured every 2.5 K with the leading 3 omitted on the labels. The composite radar reflectivity pattern has been overlain for reference.

convective line are feeding the high-θ_e updrafts, while behind the convective line the θ_e values immediately drop, indicating that this region consists of low-θ_e air from downdrafts. A narrow region of rear-to-front flow undoubtedly occurred near the front edge of the convective line in association with the surface gust front. The wind analysis, however, is too coarse to resolve this feature that would separate the inflow and outflow streamlines. Since the across-line component of flow is so dominant at the surface, it is difficult to discern variations in the flow in Fig. 15a. Therefore, the *ground-relative* flow, which shows the structure more clearly, is presented in Fig. 15b.

This flow is characterized by strong diffluence concentrated in the center of the secondary precipitation band. Figure 15c confirms that divergence in the stratiform region was also centered on the secondary band. These patterns further indicate the influence of the secondary precipitation band on the wind field (i.e., microphysical–dynamical feedback) in the stratiform region. A band of stronger divergence was found near the back of the convective line in association with outflow from strong convective downdrafts. A ridge of high pressure lay between the enhanced portions of the secondary band and the strongest parts of the convective line, with the southern part of the ridge stronger than the northern part (Fig. 15d).

Presquall mesolows were located near the northern and southern ends of the composite convective line (Fig. 15d). The mesolow at the southern end was associated with a preexisting low pressure feature and moved somewhat independently of the squall line, being highly transient in the composite framework. In contrast, the presquall mesolow at the northern end of the convective line moved with the squall line and was found in roughly the same relative location throughout the 3-h period that the mesolow was in the dense mesonetwork. This mesolow, associated with deep subsidence at mid-to-upper levels (Figs. 10c, 11c, and 12c), was located at the end of a sharp line of convergence that lay along the front of the convective line. Mesolows associated with deep subsidence aloft have been noted previously in simulations of MCS's (Fritsch and Chappell 1980).

The convergence line corresponded closely to the front edge of the surface precipitation pattern in the northern and southern portions of the storm, but was located 20–30 km ahead of the enhanced convective echo region in the central part of the convective line [from $(X', Y') = (-30, -150)$ to about $(0, -30)$ in Fig. 15c]. Vasiloff (1989) showed evidence of a fine-line reflectivity structure roughly 20 km ahead of that part of the convective line at 0400 UTC and related it to the position of the surface gust front. Figure 15e shows that the convergence line also corresponded to the front edge of the strong θ_e gradient that was associated with the gust front. The θ_e gradient associated with the gust front was strongest in the central portion of the storm and virtually nonexistent to the north of the northern presquall mesolow.

At the surface, low-θ_e air, strong divergence, and a strong high pressure perturbation was found to the *rear* of the central, or bowed-out, part of the convective line. Additionally, the *highest* surface θ_e values were found *ahead* of the bowed-out part of the convective line. As noted previously, this part of the storm was also associated with the strongest storm-relative rear-to-front flow at low levels. Inspection of the wind gusts recorded at the surface mesonet sites and reported from various towns throughout Kansas and Oklahoma revealed that a swath, 150 km wide and 400 km long, of winds in excess of 26 m s^{-1} occurred in association with the central segment of the convective line. These data satisfy the size and strength criteria set forth in Johns and Hirt (1987) for a *derecho* (strong, straight-line wind) event. A study currently underway indicates that a progressive derecho developed during the early stages of the 10–11 June 1985 storm. The derecho lasted for approximately 8 h and was limited to the central part of the convective line.

7. Physical distinction of the mesoscale updrafts and downdrafts

At each pressure level in the composite analysis, the vertical velocity was averaged horizontally using the composite radar reflectivity structure (Fig. 6d) to set the boundaries of the convective and stratiform regions. The convective region had mean ascent throughout the troposphere with a peak upward motion of about 90 cm s^{-1} near 400 mb (Fig. 16a). In the stratiform region, mean ascent, with a maximum of 30 cm s^{-1} near 300 mb, was found at upper levels with mean subsidence at mid-to-lower levels. The level of the zero mean vertical velocity was located just above the melting level. The depth and strength of the stratiform region updrafts and downdrafts observed in this storm are similar to those obtained in previous studies of squall-line systems (Houze 1989).

The comprehensive composite analysis discussed here includes high-resolution Doppler radar data over a large portion of the storm system—from the leading edge of the convective line to the rear edge of the stratiform precipitation. Such complete cross-storm Doppler radar coverage has not been previously available. This broad coverage, together with the high resolution of the radar data, allowed us to subdivide the stratiform precipitation region into three parts. This subdivision constitutes an attempt to investigate the relationship between precipitation intensity and the spatial structure of the mesoscale updrafts and downdrafts. Based on the composite radar reflectivity structure, the three subdivisions identified are the stratiform region excluding any part of the secondary band (SNSB), the secondary band excluding the most enhanced portions

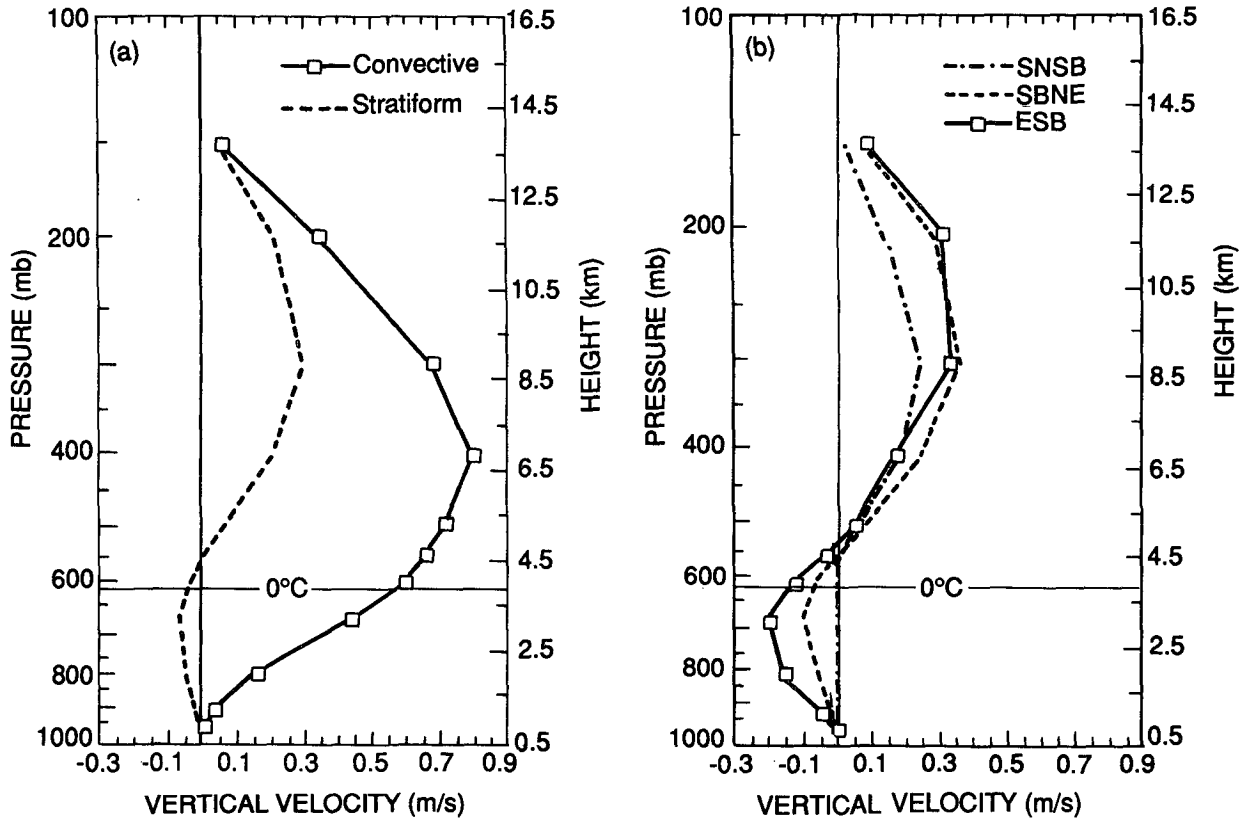

FIG. 16. Mean vertical velocity for (a) convective (solid) and entire stratiform (dashed) regions, (b) stratiform region excluding the secondary band (SNSB), secondary band excluding the enhanced portions (SBNE), and enhanced portions of the secondary band (ESB). The height of the 0°C level is also shown.

(SBNE), and the most enhanced portions of the secondary band (ESB).

Figure 16b shows the vertical profiles of mean vertical motion for each subregion. The mesoscale downdraft was most pronounced in the area associated with the strongest precipitation and was, on average, virtually nonexistent in the weak stratiform precipitation regions. In contrast, the mesoscale updraft was more equally distributed throughout all parts of the stratiform region. Since the SNSB profile represents an average over both the transition zone to the rear of the convective line and the rear of the stratiform region where the precipitation was weak, it is likely that aliasing from the convective region in the southern part of the storm reduced the strength of the mesoscale downdraft in the SNSB profile. Still, the EVAD analyses of Rutledge et al. (1988a) indicate that the strongest downward motion observed in the stratiform region of the squall-line system was associated with the heaviest stratiform precipitation. Additionally, a distinction is made between the "common" mesoscale downdraft driven by evaporational cooling (Brown 1979) and affected by melting (Leary and Houze 1979) that appears to be characteristic of squall-line systems (Houze 1989), and the subsidence at the rear of the stratiform region that is associated with the intrusion of relatively dry rear inflow that apparently does not occur in all squall-line systems (Smull and Houze 1987b). With this distinction in mind, the mesoscale downdraft was apparently a smaller-scale feature than the mesoscale updraft. Previously the mesoscale updrafts and downdrafts have been treated as single bulk entities of essentially the same scale. The breadth of the mesoscale updraft indicates that the mean upward motion may have been associated with the large-scale buoyancy of the trailing stratiform *cloud,* while the strong correlation between the strength of the mesoscale downdraft and the intensity of the stratiform precipitation indicates that the mesoscale downdraft was more associated with the stratiform *precipitation.* The location of the strongest downward motion, just below the melting level, further suggests that cooling associated with melting (Leary and Houze 1979) was a major contributor to the downward motion.

8. Precipitation structure in relation to the relative flow

a. Calculation of hydrometeor trajectories

The horizontal and vertical air motions described in section 6 were combined with estimates of particle

fall speeds (appendix C) to calculate trajectories of precipitation through the storm system. Fall speeds of the precipitation particles behind the convective line were assumed to be those determined by the EVAD analyses reported in Rutledge et al. (1988a). For the convective region, where no such direct determination was possible, the radar reflectivity versus the fall-speed relationship discussed in section 3 was used.

b. *Overall width of the trailing stratiform region*

Trajectories of ice particles, calculated backward in time from the melting level at the rear edge of the stratiform region and forward in time from 150 mb at the rear of the convective region, indicate that the *width* of the trailing region of stratiform precipitation was controlled by a combination of microphysical and relative wind velocity scales, as suggested previously by Houze (1981), Smull and Houze (1985), and Rutledge and Houze (1987). Trajectories in Fig. 17a show that the distance traveled rearward by ice ejected from the convective region depended on both the strength of the relative flow and the time required for the particle to reach the melting level. The 2–3-h period needed for an ice particle to travel from 150 mb to the melting level, combined with the velocity of the relative flow, yields the ~150-km horizontal width of the trailing stratiform precipitation region.

c. *The region of heaviest stratiform precipitation*

The enhanced portions of the secondary band, that is, the regions of heaviest stratiform precipitation, were located directly downwind of the most intense portions of the convective region, which were probably the greatest sources of ice particles being advected rearward into the stratiform region (Fig. 17b). Moreover, the backward trajectories from the enhanced portions of the secondary band passed through regions of strong upward motion at mid-to-upper levels (compare Fig. 17b with Figs. 9c, 10, 11c, and 12c). In a kinematic modeling study of a similar storm by Rutledge and Houze (1987), the influence of ice particles from the convective into the stratiform region and the growth of these particles as they pass through a region of mesoscale ascent were recognized as the important factors explaining the location and intensity of the enhanced stratiform precipitation. They found that while 80% of the mass of the stratiform precipitation was due to condensation produced by the mesoscale updraft, almost no rain would have reached the surface in the stratiform area without the influx of ice from the convective region. Thus, the occurrence of the enhanced stratiform precipitation constituting the secondary band was apparently the result of a cooperative process in which the ice particles were supplied by the intense portions of the convective region and increased in mass by condensation in the strong mesoscale updraft at upper levels in the stratiform region before they reached the melting level.

d. *The effect of the rear-to-front flow*

Another important feature that affected the precipitation structure of the storm was the dry rear-to-front flow at mid-to-lower levels in the northern portion of the storm system. Some precipitation trajectories extended from the enhanced portions of the convective line and passed through broad regions of mesoscale ascent, but ended in relatively weak portions of the stratiform precipitation area (Fig. 17c). The difference between these trajectories and those shown in Fig. 17b is that these trajectories passed into the extremely dry rear-to-front flow at mid-to-lower levels in the northern portion of the storm system behind the heaviest stratiform precipitation region (compare Fig. 17c with Figs. 12a, 13a, and 14a). Evaporation, or sublimation above the melting level, in the dry rear-to-front flow was apparently sufficient to greatly reduce the rainfall in that part of the storm.

9. The "reflectivity trough"

At low levels, weak reflectivity was observed between the enhanced portion of the secondary band and the rear of the convective line. In a study of a similar squall-line system, Ligda (1956) termed this region the "dry slot," but it is more often referred to as the "transition zone" (Smull and Houze 1985) or the "reflectivity trough" (Sommeria and Testud 1984). In this paper, transition zone refers to the entire region between the rear of the convective line and the secondary band, while reflectivity trough refers to the radar reflectivity minimum commonly observed at low levels in the transition zone. The reflectivity trough could be explained microphysically in terms of the fall-speed sorting of hydrometeors as they are ejected rearward from the convective region with the heavy particles falling nearly vertically and the light particles being carried some distance back by the front-to-rear relative flow, or explained dynamically by deep subsidence in the transition zone, creating an unfavorable environment for growth of the falling hydrometeors and possibly reducing their mass through sublimation and evaporation. Both processes were apparently active in the 10–11 June 1985 storm.

Hydrometeor fall speeds at upper levels in the transition zone were not significantly different from those observed elsewhere at upper levels in the stratiform region (appendix C). Moreover, backward trajectories indicate that most of the hydrometeors at the melting level in the transition zone came from the 300–400-mb level in the convective region (Fig. 17d). To have come from levels above 300 mb, the hydrometeors would have needed greater fall speeds than the average values indicated by the EVAD analysis near the convective region (appendix C). Since hydrometeors near

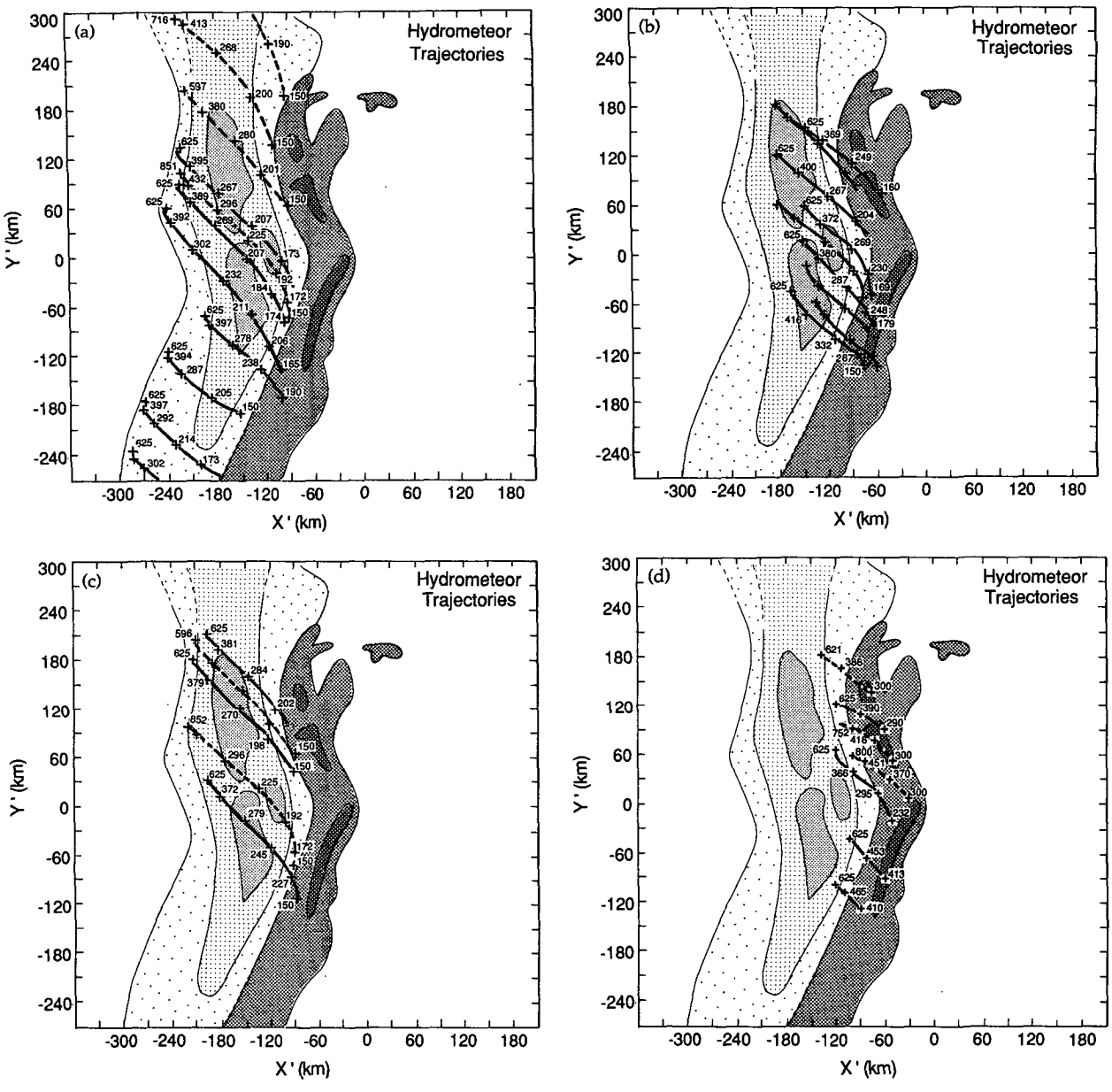

FIG. 17. Precipitation-particle trajectories (a)–(d) through the 10–11 June 1985 squall-line system. Solid lines indicate backward trajectories and dashed lines indicate forward trajectories. Pressure levels along the trajectories are given to the nearest millibar. Time intervals (30 min) along each trajectory are indicated by "+."

storm top (150 mb) apparently did not contribute to the precipitation at midlevels in the transition zone and few, if any, heavy hydrometeors were present at upper levels in the transition zone, fall-speed sorting must have been active in the 10–11 June 1985 storm.

In addition to fall-speed sorting, forward trajectories from the convective region at 300 mb and backward trajectories from the melting level in the transition zone indicate that many of the ice particles reaching the melting level in the transition zone passed through a layer of subsidence that was found between the rear of the convective line and the enhanced portions of the secondary band (compare Fig. 17d with Figs. 10c, 11c, 12c, and 13d). The vertical motions observed in this region of the storm have been verified in a higher-resolution composite study made exclusively from Doppler radar data (Biggerstaff and Houze 1991b). Enhanced subsidence in this part of the storm was also observed in the modeling study of ZGP. Moreover, Smull and Houze (1987a) noted strong mid-to-lower-level subsidence in the transition zone of a similar storm. Without a mesoscale region of ascent, the par-

ticles in the transition zone were apparently unable to grow. Sublimation and evaporation in the subsidence layer may have even reduced the mass of the falling particles. Hence, the reflectivity at mid-to-low levels in the transition zone was weaker than that in the trailing stratiform region where condensation in the mesoscale updraft was able to contribute significantly to the mass of the stratiform precipitation.

While it is apparent that both fall-speed sorting and deep subsidence in the transition zone occurred in the 10–11 June 1985 storm, the trajectory analysis presented here suggests a third possible explanation for the reflectivity trough. Namely, the hydrometeor source region for the transition zone was found at a lower altitude (300–400 mb) than that for the secondary band (about 150 mb). This difference in altitude of the source region could affect the low-level reflectivity in the transition zone by reducing the time required for ice particles to travel from the convective line to the melting level. Hence, even if a mesoscale updraft had been present at mid-to-upper levels in the transition zone, the particles in that region would have had less opportunity to grow than the particles found further back in the secondary band, which had traveled for a longer period of time. A fourth possible factor, also related to the difference in altitude of the hydrometeor source region, is that the amount of detrainment of ice particles between 300 and 400 mb might have been less than that aloft, in which case fewer hydrometeors would be expected at low levels in the transition zone than in the secondary band.

10. Conclusions

A comprehensive composite analysis of the mature phase of the leading-line trailing stratiform mesoscale convective system (MCS) that occurred on 10–11 June 1985 over Kansas and Oklahoma has been conducted by combining high-frequency rawinsonde, profiler, surface mesonetwork, and dual-Doppler radar data in a coordinate system attached to the moving storm. This study marks the first time that a series of high-resolution dual-Doppler analyses covering the entire breadth of an MCS (over a 200×300 km^2 area) have been combined with other types of data in a single analysis framework. The objective of this research was to produce a comprehensive analysis of the kinematics and precipitation structure of this type of storm, that is, an analysis that attempts to use all of the available data simultaneously to obtain the best possible representation of the storm's structure. Inclusion of the Doppler radar data in the analysis allowed us to investigate several aspects of the trailing stratiform precipitation region that had remained unclear from previous studies.

With the high resolution of the Doppler radar data it was possible to investigate the relationship between precipitation intensity and the spatial structure of the mesoscale updrafts and downdrafts. Averages of the diagnosed vertical velocity over subdivisions of the trailing stratiform region, based on radar reflectivity, showed that the mesoscale updraft was uniformly distributed throughout the stratiform region at upper levels while the mesoscale downdraft was concentrated in the region of heaviest stratiform precipitation and was, on average, virtually nonexistent in the weak stratiform precipitation region. Thus, the mesoscale updraft was observed to have the scale of the trailing stratiform *cloud* while the mesoscale downdraft, excluding that part associated with the intrusion of relatively dry rear inflow at the rear of the stratiform region, was observed to have the scale of the trailing stratiform *precipitation.*

The relationship between the three-dimensional storm-relative flow and the trailing precipitation structure was also examined. Analysis of the precipitation and wind fields, which were observed independently, indicates that the width of the stratiform precipitation region was controlled by the horizontal distance that falling hydrometeors were advected rearward from the back of the convective line by the front-to-rear storm-relative flow above the melting level. Trajectories of precipitation particles also indicate that the position of the heaviest stratiform precipitation, referred to as the "secondary band," came directly from the most intense portions of the convective region. Moreover, the hydrometeors observed at the melting level in the secondary band had traveled through a broad region of upward motion above the melting level where condensation, produced by the upward motion, apparently helped to increase their mass.

The composite precipitation and wind fields were also used to investigate the minimum in radar reflectivity observed at mid-to-low levels between the convective region and the secondary band (i.e., the reflectivity trough in the transition zone). A conceptual model of precipitation trajectories (Fig. 18),[4] based on our analysis of the relative flow and hydrometeor fall speeds, indicates that there were three separate processes active in the 10–11 June 1985 storm that may have affected the radar reflectivity at mid-to-low levels in the transition zone. With the present dataset it is not possible to determine which, if any, process was dominant. Figure 18 illustrates fall-speed sorting, the first process, by the rearward procession of increasingly smaller hydrometeors in the convective region. Precipitation particles were generated in the updraft inflow with the largest (i.e., heaviest) particles falling to the surface before being swept out of the convective region by the relative flow and the smaller (i.e., lighter) particles being carried farther aloft.

The smallest hydrometeors were evidently carried into the upper regions of the convective cell where detrainment was intense. As the hydrometeors fell back to the surface, the front-to-rear relative flow was able

[4] The cloud shield in Fig. 18 is idealized.

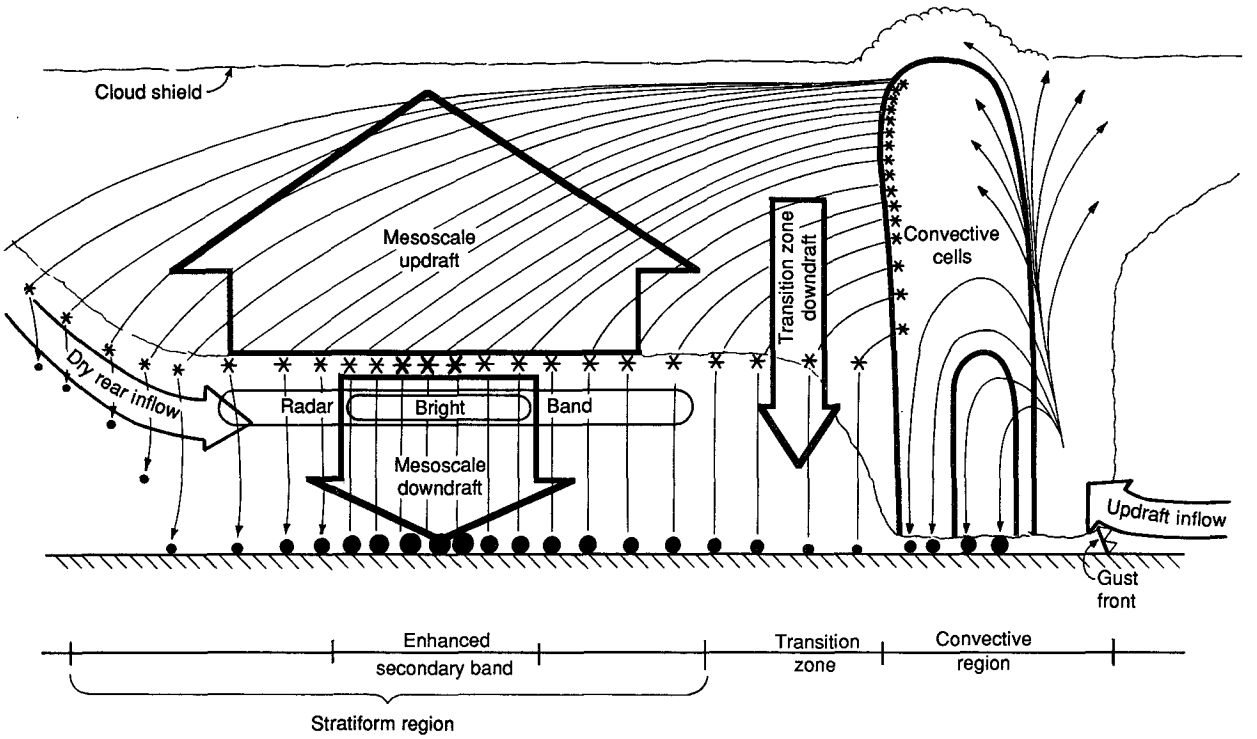

FIG. 18. Conceptual model of the two-dimensional hydrometeor trajectories through the stratiform region of a squall line with trailing stratiform precipitation. See text for further explanation.

to spread them rearward over a large horizontal distance. Assuming that the detrainment of hydrometeors occurred only near cloud top, fall-speed sorting would produce a minimum in hydrometeors at mid-to-low levels between the rear of the convective region and where the cloud-top–ejected hydrometeors settled to the surface farther back. However, detrainment was not limited to levels near cloud top. In Fig. 18, hydrometeor trajectories, represented by the thin solid lines, indicate that the source region of hydrometeors for the secondary band was at a higher altitude (150 mb) than the source region for the transition zone (300–400 mb). While the amount of rearward advection of hydrometeors (indicated in Fig. 18 by the concentration of precipitation paths) may have been less between 300 and 400 mb than at 150 mb, which was near the highly divergent storm top, the difference in hydrometeor source altitudes for particles in the secondary band and the transition zone implies a second distinct process that may have resulted in stronger reflectivities at mid-to-low levels over the secondary band than over the transition zone. Namely, the lower source region altitude for hydrometeors in the transition zone implies a shorter time period for those particles to grow before reaching the melting level. Thus, even with uniform vertical air motion throughout the stratiform region, the particles at the melting level in the secondary band would have accumulated more mass than those in the transition zone. However, the vertical air motion was not uniform. As indicated by the bold arrows in Fig. 18, deep subsidence, the third process affecting the reflectivity in the transition zone, was observed at mid-to-upper levels in the transition zone while a broad region of ascent was found above the secondary band. Sublimation and evaporation associated with the deep subsidence in the transition zone may have reduced the mass of the falling hydrometeors in that region while condensation, produced in the mesoscale updraft above the secondary band, led to enhanced mass (and, thus, enhanced radar reflectivity) in the secondary band.

Figure 18 illustrates the combined effect of all those processes affecting the precipitation structure of the 10–11 June 1985 storm by the difference in size and number of hydrometeors just above the radar bright band (associated with melting) throughout the stratiform region. As suggested by the heavy concentration of large particles in Fig. 18, the highest ice water content in the stratiform region would be found immediately above the enhanced portion of the secondary band. In a preliminary analysis of microphysical data taken just above the melting level during a level flight through the stratiform region of the 10–11 June 1985 storm, Rutledge et al. (1988b) found the highest ice water content across the secondary band. Since surface rainfall underneath the stratiform region is directly associated with hydrometeors above the melting level, the distribution of stratiform precipitation at the surface

was also affected by the processes of fall-speed sorting, differential hydrometeor source-region altitude, and nonuniform vertical air motions through the stratiform region. Additionally, as indicated near the rear of the stratiform region in Fig. 18, the dry rear-to-front relative flow in the stratiform region reduced the hydrometeor mass by evaporation and sublimation.

The comprehensive analysis presented here, derived from an assimilation of rawinsonde, Doppler radar, profiler, and surface mesonet data, is the most complete dataset available to pursue quantitative mesoscale diagnostic analysis of a squall-line system. It should be useful in assessing mass, heat, water, momentum, and vorticity budgets, and in making comparisons with model results. We have used the dataset here to clarify aspects of the precipitation structure and kinematics of the MCS. In our next paper we analyze the midlevel vorticity structure of the storm.

Acknowledgments. Professor S. A. Rutledge provided the 0414 and 0510 UTC Doppler analyses. Professor S-W. Shou performed a preliminary analysis of the rawinsonde data. Dr. D. Churchill and H. Terri transferred the Doppler radar analysis software from NCAR to the University of Washington and developed other useful software. C. Mohr, C. Mueller, and T. Matejka made many helpful suggestions in performing the Doppler analyses. G. C. Gudmundson edited the manuscript and K. M. Dewar drafted the figures. S. Braun and M.-J. Yang digitized the relative flow fields. This research was funded by the National Science Foundation under Grant ATM-8719838.

APPENDIX A

The Dual-Doppler Vertical Velocity Calculation

During the dual-Doppler analyses, vertical velocity was calculated by integrating the anelastic continuity equation

$$\nabla \cdot (\rho \mathbf{V}) = 0 \qquad \text{(A1)}$$

downward from echo top. Here ∇ is the three-dimensional gradient operator, ρ is the density that is assumed to be a function of height only, and $\mathbf{V}$ is the three-dimensional wind vector. Several different values ranging from 0 to 2 m s^{-1} in the convective region and 0 to 0.25 m s^{-1} in the stratiform region were used to determine the effect of the boundary condition on the calculated vertical velocity.

Since the radar data were collected up to 58° in elevation, the structure and area-averaged values of the vertical velocity in the convective region were not significantly affected by the different boundary conditions. The strong divergence near storm echo top was well sampled and quickly dominated the calculation of vertical velocity. Each integration also revealed that areas of high reflectivity aloft were associated with enhanced upward motion at upper levels. This suggested that the boundary condition should be reflectivity dependent. Hence, a boundary condition (BC) in the form:

$$\text{BC} = \begin{pmatrix} \text{C1 if dBZ} \geq \text{DZT for height} \geq H \\ \text{C2 otherwise} \end{pmatrix} \qquad \text{(A2)}$$

was chosen. Many combinations were tested before finally selecting C1 = 0.25 m s^{-1}, DZT = 10 dBZ, H = 13.9 km above mean sea level (MSL), and C2 = 0 m s^{-1}. The results were not sensitive to slight variations in any of these values. This combination was selected because the area-averaged vertical velocity near the ground was close to zero. A zero-mean vertical velocity near the ground is a good indication that only random errors were present in the vertical-velocity calculation. Since a poor boundary condition represents a nonrandom error, a zero-mean vertical velocity near the ground indicates that the upper-level boundary condition was well chosen.

In the stratiform region, the area-averaged vertical velocity was sensitive to the value of the boundary condition applied at echo top. Unlike the convective region, the upper-level divergence in the stratiform region was not strong enough to overcome the differences in the applied boundary conditions. Analyses at echo top also revealed some variation in strength of the divergence across the stratiform region. Generally, regions of enhanced divergence at storm top were associated with enhanced upward motion. Thus, a boundary condition that took into account the locations of enhanced divergence at echo top was desired. The form of the boundary condition became:

$$\text{BC} = \text{H1}\, D_{\text{top}} \qquad \text{(A3)}$$

where D_{top} is the uppermost divergence measurement in each grid column and H1 is a user-specified constant. Equation (A3) can also be interpreted as the result of integrating the anelastic continuity equation from Z_o to (Z_o − H1) assuming that the mass flux is constant and that w = 0 m s^{-1} at Z_o, which is H1 meters above the level of uppermost divergence. Thus, H1 has units of length. The use of (A3) allowed the storm to select its own boundary condition at each grid column under the uniform constraint given by H1. Various values of H1 ranging from 100 m to 2 km were tested. The mean vertical velocity near the ground was closest to zero for H1 = 250 m. Using that value, the boundary conditions ranged from ±5 cm s^{-1}.

APPENDIX B

Modified O'Brien Adjustment Scheme

To integrate the pressure-coordinate continuity equation

$$\frac{\partial u}{\partial x} + \frac{\partial v}{\partial y} + \frac{\partial \omega}{\partial p} = 0 \qquad \text{(B1)}$$

a single boundary condition (BC) at either the upper or lower boundary is needed. Generally, the uncertainty in vertical motion diagnosed from (B1) increases away from the boundary due to the accumulation of errors in the divergence of the measured horizontal winds at each level. O'Brien (1970) suggested that an additional constraint be applied at the second boundary to reduce this uncertainty. Thus, constraints were applied at both boundaries in the comprehensive composite analysis of vertical motion.

At the surface, the geometric vertical velocity w was set to zero. Since the storm is assumed to be steady in the composite coordinate system, the lower BC becomes:

$$\omega_o = u\frac{\partial p}{\partial x} + v\frac{\partial p}{\partial y} \qquad \text{(B2)}$$

where p is the surface pressure. The composite surface mesonet data were used in (B2) to calculate ω_o. The divergence was then integrated upward from the surface using the composite surface-pressure field to determine the depth of the first step of integration.

Previous studies have set ω_o to zero at the surface (Ogura and Liou 1980; Johnson et al. 1990; and others). Setting the geometric versus the pressure-coordinate vertical velocity to zero at the surface made little difference for the 10–11 June 1985 storm. Translated to storm top, the area-averaged difference was only about 2 cm s^{-1} over the stratiform region.

The cloud top for the 10–11 June 1985 storm was between 150 and 200 mb for the stratiform region and between 125 and 150 mb for the convective region (Johnson and Hamilton 1988; Rutledge et al. 1988a). Thus, the composite analysis storm top, where a second BC was applied, was taken to be at 150 mb. A variation of the scheme suggested by O'Brien (1970) was used to apply the second BC at storm top.

Assuming that the divergence at 150 mb was constant over a 10-mb depth, (B1) was integrated downward from 140 mb, where $\omega = 0$ was imposed, to calculate the vertical motion at 150 mb. This method, necessary because the divergence above 150 mb was not adequately sampled, is similar to that used to derive the upper BC in the stratiform-region dual-Doppler analyses (appendix A). Since this technique allows regions of strong divergence at cloud top to have more residual upward motion than other regions of the storm, it is more flexible than the standard O'Brien (1970) adjustment, which employs a constant vertical motion everywhere at the second boundary. A major disadvantage to this technique, hereafter referred to as the modified O'Brien scheme, is that the vertical motion at cloud top is determined solely from the measured divergence present there. Thus, the uncertainty at this level is directly proportional to the uncertainty of the upper-level horizontal wind measurements. Still, this method is preferred over applying a uniform second boundary well above cloud top and integrating over a deep layer where the divergence estimates are most uncertain.

APPENDIX C

Estimates of Hydrometeor Fall Speeds

Fall speeds of the precipitation particles behind the convective line were assumed to be those determined from the EVAD analyses reported in Rutledge et al. (1988a). Table C1 lists the profiles of hydrometeor fall speeds used in the transition zone (TZ), the secondary band (excluding the enhanced portions—SBNE), the enhanced portions of the secondary band (ESB), and the weaker stratiform precipitation behind the secondary band (WS). The TZ profile was based on the 0254 UTC CP3 EVAD analysis while the SBNE profile was based on the 0334 UTC CP3 analysis. The ESB profile was obtained by averaging the 0350 and 0420 UTC CP4 analyses, while the WS profile was obtained by averaging the 0322, 0350, and 0419 UTC CP3 analyses with the 0447 UTC CP4 analysis. Since some profiles were based on a single observation while others were based on several, small differences in the fall speeds across the storm are not deemed significant.

In the convective region, the fall speed–reflectivity relationship discussed in section 3 was used. The vertical profile of radar reflectivity in the convective region was determined from an average of the CP3 and CP4 radar data. Table C2 lists the reflectivity and fall-speed profiles used over the convective region.

The three-dimensional fall-speed field in the composite framework was then constructed by assigning each grid column a profile of particle fall speed based on the low-level radar reflectivity structure of the storm. Each grid column in the convective region was assigned the convective profile; each grid column in the enhanced secondary band was assigned the ESB profile; each grid column outside the surface rainfall pattern was assigned a zero; etc. Thus, horizontal gradients in hydrometeor fall speeds exist only at the boundaries separating the various reflectivity regions of the storm.

TABLE C1. EVAD-derived particle fall speeds in meters per second (from Rutledge et al. 1988a).

p (mb)	TX	SBNE	ESB	WS
900	6.0	7.0	7.6	6.7
800	8.5	7.0	8.1	7.5
675	8.0	6.5	5.0	5.8
600	3.0	2.3	2.0	1.6
550	1.9	2.5	2.1	1.8
500	1.7	2.3	1.8	2.3
400	1.6	2.0	1.6	1.3
300	1.4	1.7	1.3	1.4
200	1.0	1.0	0.9	0.8
150	0.8	0.7	0.5	0.5

TABLE C2. Reflectivity and fall speed profiles for the convective region.

p (mb)	Reflectivity (dBZ)	Fall speed (m s^{-1})
900	33.0	6.1
800	34.0	6.6
675	33.9	5.7
600	31.8	1.6
550	31.0	1.6
500	30.2	1.7
400	28.4	1.8
300	24.0	1.8
200	14.3	1.8
150	6.3	1.7

REFERENCES

Augustine, J. A., and E. J. Zipser, 1987: The use of wind profilers in a mesoscale experiment. *Bull. Amer. Meteor. Soc.*, **68,** 4–17.

Battan, L. J., 1973: *Radar Observation of the Atmosphere.* University of Chicago Press, 324 pp.

Biggerstaff, M. I., and R. A. Houze, Jr., 1991a: Midlevel vorticity structure of the 10–11 June 1985 PRE-STORM squall line. *Mon. Wea. Rev.*, **119,** 3066–3079.

——, and ——, 1991b: Kinematic and microphysical structure of the transition zone of a midlatitude squall line. *J. Atmos. Sci.*,submitted.

Bluestein, H. B., and M. H. Jain, 1985: Formation of mesoscale lines of precipitation: Severe squall lines in Oklahoma during the spring. *J. Atmos. Sci.*, **42,** 1711–1732.

——, G. T. Marx and M. H. Jain, 1987: Formation of mesoscale lines of precipitation: Nonsevere squall lines in Oklahoma during the spring. *Mon. Wea. Rev.*, **115,** 2719–2727.

Brandes, E. A., 1990: Evolution and structure of the 6–7 May 1985 mesoscale convective system and associated vortex. *Mon. Wea. Rev.*, **118,** 109–127.

Brown, J. M., 1979: Mesoscale unsaturated downdrafts driven by rainfall evaporation: A numerical study. *J. Atmos. Sci.*, **36,** 313–338.

Chong, M., P. Amayenc, G. Scialom and J. Testud, 1987: A tropical squall line observed during the COPT 81 experiment in West Africa. Part I: Kinematic structure inferred from dual-Doppler radar data. *Mon. Wea. Rev.*, **115,** 670–694.

Cunning, J. B., 1986: The Oklahoma–Kansas Preliminary Regional Experiment for STORM-Central. *Bull. Amer. Meteor. Soc.*, **67,** 1478–1486.

Dudhia, J., M. W. Moncrieff and D. W. K. So, 1987: The two-dimensional dynamics of West African squall lines. *Quart. J. Roy. Meteor. Soc.*, **113,** 121–146.

Fovell, R. G., and Y. Ogura, 1988: Numerical simulation of a midlatitude squall line in two dimensions. *J. Atmos. Sci.*, **45,** 3846–3879.

——, and ——, 1989: Effect of vertical wind shear on numerically simulated multicell storm structure. *J. Atmos. Sci.*, **46,** 3144–3176.

Fritsch, J. M., and C. G. Chappell, 1980: Numerical prediction of convectively driven mesoscale pressure systems. Part II: Mesoscale model. *J. Atmos. Sci.*, **37,** 1734–1762.

——, R. J. Kane and C. R. Chelius, 1986: The contribution of mesoscale convective weather systems to the warm-season precipitation in the United States. *J. Climate Appl. Meteor.*, **25,** 1333–1345.

Fujita, T. T., 1955: Results of detailed synoptic studies of squall lines. *Tellus,* **7,** 405–436.

Gamache, J. F., and R. A. Houze, Jr., 1982: Mesoscale air motions associated with a tropical squall line. *Mon. Wea. Rev.*, **110,** 118–135.

——, and ——, 1985: Further analysis of the composite wind and thermodynamic structure of the 12 September GATE squall line. *Mon. Wea. Rev.*, **113,** 1241–1259.

Hamilton, R. A., and J. W. Archbold, 1945: Meteorology of Nigeria and adjacent territory. *Quart. J. Roy. Meteor. Soc.*, **83,** 303–314.

Hauser, D., F. Roux and P. Amayenc, 1988: Comparison of two methods for the retrieval of thermodynamic and microphysical variables from Doppler-radar measurements: Application to the case of a tropical squall line. *J. Atmos. Sci.*, **45,** 1285–1303.

Heymsfield, G. M., and S. Schotz, 1985: Structure and evolution of a severe squall line over Oklahoma. *Mon. Wea. Rev.*, **113,** 1563–1589.

Houze, R. A., Jr., 1981: Structure of atmospheric precipitation systems—a global survey. *Radio Sci.*, **16,** 671–689.

——, 1989: Observed structure of mesoscale convective systems and implications for large-scale heating. *Quart. J. Roy. Meteor. Soc.*, **115,** 425–461.

——, and E. N. Rappaport, 1984: Air motions and precipitation structure of an early summer squall line over the eastern tropical Atlantic. *J. Atmos. Sci.*, **41,** 553–574.

——, S. A. Rutledge, M. I. Biggerstaff and B. F. Smull, 1989: Interpretation of Doppler weather-radar displays of midlatitude mesoscale convective systems. *Bull. Amer. Meteor. Soc.*, **70,** 608–619.

——, B. F. Smull and P. Dodge, 1990: Mesoscale organization of springtime rainstorms in Oklahoma. *Mon. Wea. Rev.*, **118,** 613–654.

Hoxit, L. R., C. F. Chappell and J. M. Fritsch, 1976: Formation of mesolows or pressure troughs in advance of cumulonimbus clouds. *Mon. Wea. Rev.*, **104,** 1419–1428.

Johns, R. H., and W. D. Hirt, 1987: Derechos: Widespread convectively induced windstorms. *Wea. Forecasting,* **2,** 32–49.

Johnson, R. H., and P. J. Hamilton, 1988: The relationship of surface pressure features to the precipitation and airflow structure of an intense midlatitude squall line. *Mon. Wea. Rev.*, **116,** 1444–1472.

——, W. A. Gallus and M. D. Vescio, 1990: Near-tropopause vertical motions within the trailing-stratiform regions of squall lines. *J. Atmos. Sci.*, **47,** 2200–2210.

Kessinger, C. J., P. S. Ray and C. E. Hane, 1987: The Oklahoma squall line of 19 May 1977. Part I: A multiple Doppler analysis of convective and stratiform structure. *J. Atmos. Sci.*, **44,** 2840–2864.

Lafore, J.-P., and M. W. Moncrieff, 1989: A numerical investigation of the organization and interaction of the convective and stratiform regions of tropical squall lines. *J. Atmos. Sci.*, **46,** 521–544.

Leary, C. A., and R. A. Houze, Jr., 1979: Melting and evaporation of hydrometeors in precipitation from anvil clouds of deep tropical convection. *J. Atmos. Sci.*, **36,** 669–679.

——, and E. N. Rappaport, 1987: The life cycle and internal structure of a mesoscale convective complex. *Mon. Wea. Rev.*, **115,** 1503–1527.

Leise, J. A., 1981: A multi-dimensional scale-telescoped filter and data extension package. NOAA Tech. Memo, WPL-82, 20 pp.

LeMone, M. A., 1983: Momentum transport by a line of cumulonimbus. *J. Atmos. Sci.*, **40,** 1815–1834.

Ligda, M. G. H., 1956: The radar observations of mature prefrontal squall lines in the midwestern United States. *VI Congress of Organisation Scientifique et Technique Internationale du Vol a Voile (OSTIV),* Aeronautical International Federation, St-Yan, France, 1–3.

Marks, F. D., Jr., and R. A. Houze, Jr., 1987: Inner-core structure of Hurricane Alicia from airborne Doppler-radar observations. *J. Atmos. Sci.*, **44,** 1296–1317.

Mohr, C. G., and L. J. Miller, 1983: CEDRIC—a software package for Cartesian space editing, synthesis, and display of radar fields under interactive control. Preprints, *21st Conf. on Radar Meteor.,* Edmonton, Amer. Meteor. Soc., 559–574.

——, —— and R. L. Vaughn, 1979: An economical procedure for Cartesian interpolation and display of reflectivity factor data in three-dimensional space. *J. Appl. Meteor.*, **18,** 661–670.

Moncrieff, M. W., and M. J. Miller, 1976: A theory of organized steady convection and its transport properties. *Quart. J. Roy. Meteor. Soc.*, **102,** 373–394.

Newton, C. W., 1950: Structure and mechanisms of the prefrontal squall line. *J. Meteor.*, **7,** 210–222.

Nicholls, M. E., 1987: A comparison of the results of a two-dimensional numerical simulation of a tropical squall line with observations. *Mon. Wea. Rev.*, **115,** 3055–3077.

O'Brien, J. J., 1970: Alternative solutions to the classical vertical velocity problem. *J. Appl. Meteor.*, **9,** 197–203.

Ogura, Y., and Y.-L. Chen, 1977: A life history of an intense mesoscale convective storm in Oklahoma. *J. Atmos. Sci.*, **34,** 1458–1476.

——, and M. T. Liou, 1980: The structure of a midlatitude squall line. *J. Atmos. Sci.*, **37,** 553–567.

Oye, R., and R. E. Carbone, 1981: Interactive Doppler editing software. *20th Conf. Radar Meteor.*, Boston, Amer. Meteor. Soc. 683–689.

Pedgley, D. E., 1962: A meso-synoptic analysis of the thunderstorms on 28 August 1958. *Brit. Meteor. Off., Geophys. Mem.*, **106,** 74 pp.

Redelsperger, J.-L., and J.-P. Lafore, 1988: A three-dimensional simulation of a tropical squall line: Convective organization and thermodynamic vertical transport. *J. Atmos. Sci.*, **45,** 1334–1356.

Rotunno, R., J. B. Klemp and M. L. Weisman, 1988: A theory for strong, long-lived squall lines. *J. Atmos. Sci.*, **45,** 463–485.

Roux, F., 1988: The West African squall line observed on 23 June 1981 during COPT 81: Kinematics and thermodynamics of the convective region. *J. Atmos. Sci.*, **45,** 406–426.

Rutledge, S. A., and R. A. Houze, Jr., 1987: A diagnostic modeling study of the trailing-stratiform region of a midlatitude squall line. *J. Atmos. Sci.*, **44,** 2640–2656.

——, ——, M. I. Biggerstaff and T. Matejka, 1988a: The Oklahoma–Kansas mesoscale convective system of 10–11 June 1985: Precipitation structure and single-Doppler radar analysis. *Mon. Wea. Rev.*, **116,** 1409–1430.

——, ——, A. J. Heymsfield and M. I. Biggerstaff, 1988b: Dual-Doppler and airborne microphysical observations in the stratiform region of the 10–11 June MCS over Kansas during PRE-STORM. Preprints, *Tenth Int. Cloud Physics Conf.* Ofenbach am Main: Deutshcer Wetterdienst, 705–707.

Smull, B. F., and R. A. Houze, Jr., 1985: A midlatitude squall line with a trailing region of stratiform rain: Radar and satellite observations. *Mon. Wea. Rev.*, **113,** 117–133.

——, and ——, 1987a: Dual-Doppler radar analysis of a midlatitude squall line with a trailing region of stratiform rain. *J. Atmos. Sci.*, **44,** 2128–2148.

——, and ——, 1987b: Rear inflow in squall lines with trailing-stratiform precipitation. *Mon. Wea. Rev.*, **115,** 2869–2889.

Sommeria, G., and J. Testud, 1984: COPT 81: A field experiment designed for the study of dynamics and electrical activity of deep convection in continental tropical regions. *Bull. Amer. Meteor. Soc.*, **65,** 4–10.

Srivastava, R. C., T. J. Matejka and T. J. Lorello, 1986: Doppler-radar study of the trailing-anvil region associated with a squall line. *J. Atmos. Sci.*, **43,** 356–377.

Tao, W.-K., and J. Simpson, 1989: Modeling study of a tropical squall-type convective line. *J. Atmos. Sci.*, **46,** 177–202.

Thorpe, A. J., M. J. Miller and M. W. Moncrieff, 1982: Two-dimensional convection in a non-constant shear: A model of midlatitude squall lines. *Quart. J. Roy. Meteor. Soc.*, **108,** 739–762.

Vasiloff, S. V., 1989: Vorticity dynamics of a squall line: A Doppler-radar analysis of the 10–11 June 1985 squall line. M.S. thesis, University of Oklahoma, 100 pp.

Weisman, M. L., and J. B. Klemp, 1982: The dependence of numerically simulated convective storms on wind shear and buoyancy. *Mon. Wea. Rev.*, **110,** 504–520.

Zhang, D.-L., and K. Gao, 1989: Numerical simulation of an intense squall line during 10–11 June 1985 PRE-STORM. Part II: Rear inflow, surface pressure perturbations, and stratiform precipitation. *Mon. Wea. Rev.*, **117,** 2067–2094.

——, —— and D. B. Parsons, 1989: Numerical simulation of an intense squall line during 10–11 June 1985 PRE-STORM. Part I: Model verification. *Mon. Wea. Rev.*, **117,** 960–994.

Zipser, E. J., 1969: The role of organized unsaturated convective downdrafts in the structure and rapid decay of an equatorial disturbance. *J. Appl. Meteor.*, **8,** 799–814.

——, 1988: The evolution of mesoscale convective systems: Evidence from radar and satellite observations. *Tropical Rainfall Measurements,* J. S. Theon, and N. Fugono, Eds., Deepak Publ., 159–166.